Progress In Electromagnetics Research, PIER 8, 377–426, 1994

DIFFRACTION BY A PARALLEL-PLATE WAVEGUIDE CAVITY WITH DIELECTRIC/FERRITE LOADING: PART I – THE CASE OF E POLARIZATION

K. Kobayashi, S. Koshikawa, and A. Sawai

1. Introduction

Analysis of the scattering from open-ended metallic waveguide cavities has received much attention recently in connection with the prediction and reduction of the radar cross section (RCS) of a target [1–7]. This problem serves as a simple model of duct structures such as jet engine intakes of aircrafts and several cracks occurring on surfaces of general complicated bodies. Therefore, investigation of the scattering mechanism in case of the existence of open cavities is an important subject in the field of the RCS prediction and reduction. Some of the cavity diffraction problems have been analyzed thus far using various

analytical and numerical methods [8–17]. Most of these approaches incorporate the scattering from the interior of the cavity including the rim diffraction at the open end, but they do not rigorously take into account the scattering effect arising from the entire exterior surface of the cavity. Hence, final solutions due to these methods appear to be valid only for the restricted range of incidence and observation angles. In addition, these solutions may not be uniformly valid for arbitrary dimensions of the cavity.

The Wiener-Hopf technique [18–21] is one of the powerful approaches for analyzing wave scattering and diffraction problems involving canonical geometries; it is mathematically rigorous in the sense that the edge condition, required for the uniqueness of the solution, is explicitly incorporated into the analysis. As an example of simple two-dimensional cavity structures, we have previously considered a finite parallel-plate waveguide with a planar termination at the open end, and analyzed the diffraction of an E-polarized plane wave rigorously using the Wiener-Hopf technique [22, 23]. It has been shown via illustrative numerical examples that our final solution is valid for arbitrary incidence and observation angles as well as for arbitrary dimensions of the cavity unless the cavity depth is too small compared with the wavelength. Some comparisons with the other existing methods have also been given and the validity of those methods has been discussed. As a generalization to the problem treated in [22, 23], we have further analyzed the plane wave diffraction by a parallel-plate waveguide cavity with a thick planar termination for both E and H polarizations using the Wiener-Hopf technique [24], where the effect of finite thickness of the endplate has been explicitly taken into account. Based on numerical computations of the far field backscattering characteristics for various physical parameters, it has been confirmed that, when the aperture is in the illuminated region against the incident field, cavities formed by these straight waveguide structures generally exhibit large RCS values since the interior irradiation then gives rise to a significant contribution to the backscattering. For applications in the aircraft scattering studies, it is often required to reduce the interior irradiation from such cavities. Two methods employed for this purpose are, (i) loading the interior of the cavity with a lossy material, and (ii) shaping the cavity. In the present paper, we shall consider a parallel-plate waveguide cavity with dielectric/ferrite loading as an example of two-dimensional cavities associated with the first method, and analyze the E-polarized

plane wave diffraction rigorously using the Wiener-Hopf technique. Since the interior of the cavity is filled with material, the method of solution becomes more complicated in comparison to that in our previous papers [22–24].

In Section 2, the Fourier transform for the unknown scattered field is introduced and transformed wave equations are derived by taking the Fourier transform of the Helmholtz equation, which contain unknown inhomogeneous terms occurring due to medium discontinuities along the transform axis. In Section 3, these transformed wave equations are solved by expanding the inhomogeneous terms into the Fourier sine series and the scattered field representation in the transform domain is derived. In Section 4, the problem is formulated in terms of the simultaneous Wiener-Hopf equations satisfied by the unknown spectral functions, where the unknown Fourier expansion coefficients are also involved. In Section 5, the Wiener-Hopf equations are solved exactly in the form of integral equations in the complex domain by application of the factorization and decomposition procedure. In order to simplify these integral equations, an important relationship between the unknown Fourier coefficients and the unknown spectral functions is subsequently investigated in Section 6. In Section 7, we shall evaluate the infinite integrals occurring in the integral equations to obtain the formal solution of the Wiener-Hopf equations using the results in Section 6. It should be noted that the formal solution involves an infinite number of unknowns and some branch-cut integrals with unknown integrands. In Section 8, we shall further develop approximation procedures for determining the unknowns and evaluating the branch-cut integrals based on rigorous asymptotics with the aid of the edge condition, and derive the approximate solution to the Wiener-Hopf equations, which involves numerical inversion of appropriate matrix equations. It is to be noted that our final approximate solution is uniformly valid in incidence and observation angles as well as in cavity dimensions unless the cavity depth is too small compared with the wavelength. Subsequently, in Section 9, the derivation of the scattered field inside and outside the cavity will be discussed by taking the Fourier inverse of the solution in the transform domain. The field inside the cavity is expressed in terms of the transmitted TE modes, whereas for the field outside the cavity, a far field asymptotic expression is derived using the saddle point method. In Section 10, we shall present representative numerical examples of the monostatic RCS and

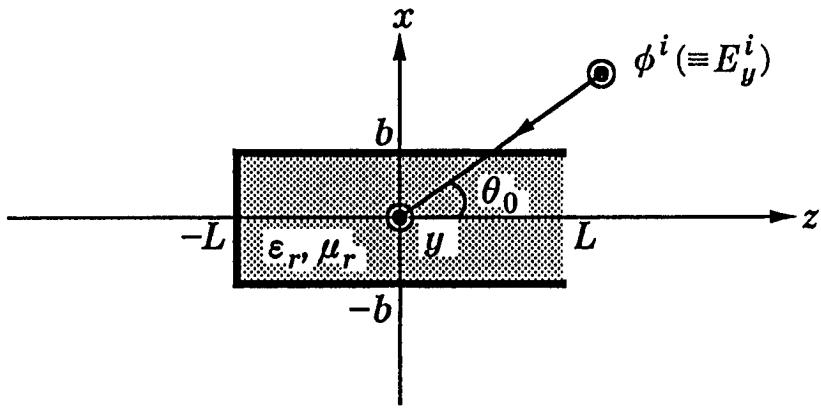

Figure 1. Geometry of the parallel-plate waveguide cavity.

the bistatic RCS for various physical parameters, and discuss the scattering characteristics of the cavity in detail. In particular, it is shown that, for large cavities, significant RCS reduction can be achieved by lossy material loading inside the cavity. Some comparisons with a high-frequency technique are also provided and the validity of that approach is discussed. Section 11 contains some concluding remarks.

The time factor is assumed to be $e^{-i\omega t}$ and suppressed throughout this paper.

2. Transformed Wave Equations

Let us consider the diffraction of an E-polarized plane electromagnetic wave by a parallel-plate waveguide cavity with dielectric/ferrite loading as shown in Fig. 1, where the E polarization implies that the incident electric field is parallel to the y-axis. The cavity plates are assumed to be infinitely thin, perfectly conducting, and uniform in the y-direction, and the medium inside the cavity is characterized by the relative permittivity ε_r and the relative permeability μ_r. The problem reduces to the one treated in our previous papers [22, 23] by letting $\varepsilon_r \to 1$ and $\mu_r \to 1$. In view of the geometry and the characteristics of the incident field, this is a two-dimensional problem.

Let the total electric field $\phi^t(x,z)[\equiv E_y^t(x,z)]$ be

$$\phi^t(x,z) = \phi^i(x,z) + \phi(x,z), \tag{1}$$

where $\phi^i(x,z)$ is the incident field of E polarization defined by

$$\phi^i(x,z) = e^{-ik(x\sin\theta_0 + z\cos\theta_0)} \tag{2}$$

for $0 < \theta_0 < \pi/2$ with $k[=\omega(\mu_0\varepsilon_0)^{1/2}]$ being the free-space wavenumber. The total field $\phi^t(x,z)$ satisfies the two-dimensional Helmholtz equation:

$$\left[\partial^2/\partial x^2 + \partial^2/\partial z^2 + \mu(x,z)\varepsilon(x,z)k^2\right]\phi^t(x,z) = 0, \tag{3}$$

where

$$\mu(x,z) = \begin{cases} 1 & \text{outside the cavity,} \\ \mu_r & \text{inside the cavity,} \end{cases} \tag{4a}$$

$$\varepsilon(x,z) = \begin{cases} 1 & \text{outside the cavity,} \\ \varepsilon_r & \text{inside the cavity.} \end{cases} \tag{4b}$$

Our problem is to determine the solution of (3) subject to appropriate boundary conditions. Nonzero components of the total electromagnetic fields are derived from the following relation:

$$(E_y^t, H_x^t, H_z^t) = \left[\phi^t,\ \frac{i}{\omega\mu_0\mu(x,z)}\frac{\partial\phi^t}{\partial z},\ \frac{1}{i\omega\mu_0\mu(x,z)}\frac{\partial\phi^t}{\partial x}\right]. \tag{5}$$

For analytical convenience, we assume the medium to be slightly lossy as in

$$k = k_1 + ik_2, \qquad 0 < k_2 \ll k_1. \tag{6}$$

The solution for real k is obtained by letting $k_2 \to +0$ at the end of analysis. It follows from the radiation condition that the scattered field satisfies

$$\phi(x,z) = O(e^{-k_2|z|\cos\theta_0}) \tag{7}$$

as $|z| \to \infty$, where the symbol O implies Landau's order notation. We now define the Fourier transform of the unknown scattered field $\phi(x,z)$ with respect to z as

$$\Phi(x,\alpha) = (2\pi)^{-1/2}\int_{-\infty}^{\infty}\phi(x,z)e^{i\alpha z}dz, \tag{8}$$

where $\alpha = \mathrm{Re}\,\alpha + i\mathrm{Im}\,\alpha(\equiv \sigma + i\tau)$. In view of (7), it is found that $\Phi(x,\alpha)$ is regular in the strip $|\tau| < k_2\cos\theta_0$ of the complex α-plane. We can also verify that $\Phi(x,\alpha)$ is bounded as $|x| \to \infty$. Introducing the Fourier integrals as

$$\Phi_{\pm}(x,\alpha) = \pm(2\pi)^{-1/2}\int_{\pm L}^{\pm\infty}\phi(x,z)e^{i\alpha(z\mp L)}dz, \tag{9a}$$

$$\Phi_1(x,\alpha) = (2\pi)^{-1/2}\int_{-L}^{L}\phi^t(x,z)e^{i\alpha z}dz, \tag{9b}$$

we can express $\Phi(x,\alpha)$ as

$$\Phi(x,\alpha) = \Psi(x,\alpha) + \Phi_1(x,\alpha), \tag{10}$$

where

$$\Psi(x,\alpha) = e^{-i\alpha L}\Psi_-(x,\alpha) + e^{i\alpha L}\Psi_{(+)}(x,\alpha), \tag{11}$$

$$\Psi_-(x,\alpha) = \Phi_-(x,\alpha) + A\frac{e^{-ikx\sin\theta_0}}{\alpha - k\cos\theta_0}, \tag{12a}$$

$$\Psi_{(+)}(x,\alpha) = \Phi_+(x,\alpha) - B\frac{e^{-ikx\sin\theta_0}}{\alpha - k\cos\theta_0}, \tag{12b}$$

$$A = \frac{e^{ikL\cos\theta_0}}{(2\pi)^{1/2}i}, \qquad B = \frac{e^{-ikL\cos\theta_0}}{(2\pi)^{1/2}i}. \tag{13}$$

In (9 a, b), $\Phi_+(x,\alpha)$ and $\Phi_-(x,\alpha)$ are regular in the upper half-plane $\tau > -k_2\cos\theta_0$ and the lower half-plane $\tau < k_2\cos\theta_0$, respectively, whereas $\Phi_1(x,\alpha)$ is an entire function. The parentheses in the subscript of $\Psi_{(+)}(x,\alpha)$ defined by (12 b) imply that $\Psi_{(+)}(x,\alpha)$ is regular in $\tau > -k_2\cos\theta_0$ except for a simple pole at $\alpha = k\cos\theta_0$. We shall henceforth use these conventions for indicating the region of regularity in the α-plane.

In order to derive transformed wave equations, we note that

$$(\partial^2/\partial x^2 + \partial^2/\partial z^2 + k^2)\phi(x,z) = 0 \tag{14}$$

and

$$(\partial^2/\partial x^2 + \partial^2/\partial z^2 + k_r^2)\phi^t(x,z) = 0 \tag{15}$$

hold outside and inside the cavity, respectively, where $k_r = (\mu_r \varepsilon_r)^{1/2} k$. For the region $|x| > b$, we can show by taking the Fourier transform of (14) and using (7) that

$$(d^2/dx^2 - \gamma^2)\Phi(x, \alpha) = 0 \tag{16}$$

holds for any α in the strip $|\tau| < k_2 \cos\theta_0$, where $\gamma = (\alpha^2 - k^2)^{1/2}$. Since γ is a double-valued function of α, a proper branch is chosen such that γ reduces to $-ik$ when $\alpha = 0$. For this branch, it is seen that $\operatorname{Re} \gamma > 0$ for any α in the strip $|\tau| < k_2$. Equation (16) is the transformed wave equation for $|x| > b$.

The derivation of transformed wave equations for the region $|x| < b$ is complicated, since there are medium discontinuities across the surfaces at $z = \pm L$. We multiply both sides of (14) by $(2\pi)^{-1/2} e^{i\alpha z}$ and integrate with respect to z over the ranges $-\infty < z < -L$ and $L < z < \infty$. Then after taking into account (7) and the boundary conditions at $z = \pm L$, we derive that

$$(d^2/dx^2 - \gamma^2)\Phi_-(x, \alpha) + f_1^-(x) - (2\pi)^{-1/2}\left[\frac{\partial \phi^i(x, -L)}{\partial z} - i\alpha\phi^i(x, -L)\right] = 0 \tag{17}$$

for $\tau < k_2 \cos\theta_0$, and that

$$(d^2/dx^2 - \gamma^2)\Phi_+(x, \alpha) - [\mu_r^{-1} f_2(x) - i\alpha g(x)] + (2\pi)^{-1/2}\left[\frac{\partial \phi^i(x, L)}{\partial z} - i\alpha\phi^i(x, L)\right] = 0 \tag{18}$$

for $\tau > -k_2 \cos\theta_0$, where

$$f_1^{\pm}(x) = (2\pi)^{-1/2} \frac{\partial \phi^t(x, -L \pm 0)}{\partial z}, \tag{19a}$$

$$f_2(x) = (2\pi)^{-1/2} \frac{\partial \phi^t(x, L - 0)}{\partial z}, \tag{19b}$$

$$g(x) = (2\pi)^{-1/2} \phi^t(x, L). \tag{19c}$$

Simple manipulation shows that

$$(d^2/dx^2 - \gamma^2)\begin{Bmatrix} A \\ B \end{Bmatrix} \frac{e^{-ikx\sin\theta_0}}{\alpha - k\cos\theta_0}$$
$$+ (2\pi)^{-1/2}\left[\frac{\partial\phi^i(x, \mp L)}{\partial z} - i\alpha\phi^i(x, \mp L)\right] = 0 \qquad (20)$$

holds for all α except $\alpha = k\cos\theta_0$. Therefore, substituting (20) into (17) and (18) and taking into account (12a, b), we find that

$$(d^2/dx^2 - \gamma^2)\Psi_-(x, \alpha) = -f_1^-(x) \qquad (21)$$

for $\tau < k_2\cos\theta_0$, and that

$$(d^2/dx^2 - \gamma^2)\Psi_{(+)}(x, \alpha) = \mu_r^{-1} f_2(x) - i\alpha g(x) \qquad (22)$$

for $\tau > -k_2\cos\theta_0$ with $\alpha \neq k\cos\theta_0$. Next we multiply both sides of (15) by $(2\pi)^{-1/2}e^{i\alpha z}$ and integrate with respect to z over the range $-L < z < L$. This gives, after making use of the boundary conditions at $z = \pm L$,

$$(d^2/dx^2 - \Gamma^2)\Phi_1(x, \alpha) = e^{-i\alpha L} f_1^+(x) - e^{i\alpha L}[f_2(x) - i\alpha g(x)] \qquad (23)$$

for all α, where $\Gamma = (\alpha^2 - k_r^2)^{1/2}$. A proper branch for Γ is chosen such that Γ reduces to $-ik_r$ when $\alpha = 0$. Equations (21)–(23) are the desired transformed wave equations for $|x| < b$.

3. Field Representation in the Transform Domain

As mentioned earlier, $\Phi(x, \alpha)$ is bounded for $|x| \to \infty$ and hence, it can be shown that the solution of (16) is expressed as

$$\Phi(x, \alpha) = \begin{cases} \Psi(b, \alpha)e^{-\gamma(x-b)} & \text{for } x > b, \\ \Psi(-b, \alpha)e^{\gamma(x+b)} & \text{for } x < -b, \end{cases} \qquad (24)$$

where we have used the following boundary conditions for tangential electric fields across $x = \pm b$:

$$\Phi_-(\pm b + 0, \alpha) = \Phi_-(\pm b - 0, \alpha)[\equiv \Phi_-(\pm b, \alpha)], \qquad (25a)$$

$$\Phi_+(\pm b + 0, \alpha) = \Phi_+(\pm b - 0, \alpha)[\equiv \Phi_+(\pm b, \alpha)], \tag{25b}$$

$$\Phi_1(\pm b + 0, \alpha) = \Phi_1(\pm b - 0, \alpha) = 0. \tag{25c}$$

Equation (24) gives a field representation in the Fourier transform domain for the region $|x| > b$.

The derivation of a field representation for the region $|x| < b$ is complicated since the transformed wave equations (21)–(23) contain the unknown inhomogeneous terms $f_1^{\pm}(x), f_2(x)$, and $g(x)$ as defined by (19 a, b, c). First we shall look for a solution of (21). Since (21) is an inhomogeneous differential equation, we can express the solution as

$$\Psi_-(x, \alpha) = \Psi_-(b, \alpha)\frac{\sinh \gamma(x+b)}{\sinh 2\gamma b} - \Psi_-(-b, \alpha)\frac{\sinh \gamma(x-b)}{\sinh 2\gamma b} - \left[F_1^-(x, \alpha) - F_1^-(b, \alpha)\frac{\sinh \gamma(x+b)}{\sinh 2\gamma b}\right] \tag{26}$$

by making use of (25 a), where $F_1^-(x, \alpha)$ is the particular solution defined by

$$F_1^-(x, \alpha) = \frac{1}{\gamma}\int_{-b}^{x} f_1^-(t)\sinh \gamma(x-t)dt. \tag{27}$$

Now, $f_1^-(x)$ is differentiable for $|x| < b$, and in view of the edge condition, it is absolutely integrable for $|x| \leq b$. Therefore, we can expand $f_1^-(x)$ into the convergent Fourier sine series as in

$$f_1^-(x) = \frac{1}{b}\sum_{n=1}^{\infty} f_{1n}^- \sin \frac{n\pi}{2b}(x+b) \tag{28}$$

for $|x| < b$. It should be noted here that the behavior of this Fourier series for $x \to \pm b \mp 0$ is governed by the edge condition. When (28) is substituted into (27), the resultant equation can be evaluated integrating term by term according to the theory of Fourier series. Thus we derive that

$$F_1^-(x, \alpha) = -\frac{1}{b}\sum_{n=1}^{\infty}\frac{f_{1n}^-}{\alpha^2 + \gamma_n^2}\sin \frac{n\pi}{2b}(x+b) + \frac{\sinh \gamma(x+b)}{\gamma b}\sum_{n=1}^{\infty}\frac{n\pi}{2b}\frac{f_{1n}^-}{\alpha^2 + \gamma_n^2}, \tag{29}$$

where $\gamma_n = [(n\pi/2b)^2 - k^2]^{1/2}$. Substituting (29) into (26) now gives,

$$\Psi_-(x,\alpha) = \Psi_-(b,\alpha)\frac{\sinh\gamma(x+b)}{\sinh 2\gamma b} - \Psi_-(-b,\alpha)\frac{\sinh\gamma(x-b)}{\sinh 2\gamma b} + \frac{1}{b}\sum_{n=1}^{\infty}\frac{f_{1n}^-}{\alpha^2+\gamma_n^2}\sin\frac{n\pi}{2b}(x+b) \tag{30}$$

for $\tau < k_2\cos\theta_0$.

We also expand $f_1^+(x)$, $f_2(x)$, and $g(x)$ in (19a,b,c) using the convergent Fourier sine series as

$$f_1^+(x) = \frac{1}{b}\sum_{n=1}^{\infty} f_{1n}^+ \sin\frac{n\pi}{2b}(x+b), \tag{31a}$$

$$f_2(x) = \frac{1}{b}\sum_{n=1}^{\infty} f_{2n} \sin\frac{n\pi}{2b}(x+b), \tag{31b}$$

$$g(x) = \frac{1}{b}\sum_{n=1}^{\infty} g_n \sin\frac{n\pi}{2b}(x+b) \tag{31c}$$

for $|x| < b$. Then by applying a procedure similar to that employed to obtain (30), we arrive at the solutions of (22) and (23) with the result that

$$\Psi_{(+)}(x,\alpha) = \Psi_{(+)}(b,\alpha)\frac{\sinh\gamma(x+b)}{\sinh 2\gamma b} - \Psi_{(+)}(-b,\alpha)\frac{\sinh\gamma(x-b)}{\sinh 2\gamma b} - \frac{1}{b}\sum_{n=1}^{\infty}\frac{c_n^+(\alpha)}{\alpha^2+\gamma_n^2}\sin\frac{n\pi}{2b}(x+b) \tag{32}$$

for $\tau > -k_2\cos\theta_0$ with $\alpha \neq k\cos\theta_0$, and

$$\Phi_1(x,\alpha) = -\frac{1}{b}\sum_{n=1}^{\infty}\frac{e^{-iaL}f_{1n}^+ - e^{iaL}c_n^-(\alpha)}{\alpha^2+\Gamma_n^2}\sin\frac{n\pi}{2b}(x+b) \tag{33}$$

for all α, where $\Gamma_n = [(n\pi/2b)^2 - k_r^2]^{1/2}$, and

$$c_n^+(\alpha) = \mu_r^{-1}f_{2n} - i\alpha g_n, \qquad c_n^-(\alpha) = f_{2n} - i\alpha g_n. \tag{34}$$

Hence, substitution of (30), (32), and (33) into (10) gives a field representation for $|x| < b$.

Summarizing the above results, we arrive at

$$\Phi(x,\alpha) = \begin{cases} \Psi(b,\alpha)e^{-\gamma(x-b)} & \text{for } x > b, \\ \Psi(-b,\alpha)e^{\gamma(x+b)} & \text{for } x < -b, \\ \Psi(b,\alpha)\dfrac{\sinh\gamma(x+b)}{\sinh 2\gamma b} - \Psi(-b,\alpha)\dfrac{\sinh\gamma(x-b)}{\sinh 2\gamma b} & \\ \quad + \dfrac{1}{b}\displaystyle\sum_{n=1}^{\infty} \dfrac{e^{-i\alpha L}f_{1n}^{-} - e^{i\alpha L}c_n^{+}(\alpha)}{\alpha^2+\gamma_n^2}\sin\dfrac{n\pi}{2b}(x+b) & \\ \quad - \dfrac{1}{b}\displaystyle\sum_{n=1}^{\infty} \dfrac{e^{-i\alpha L}f_{1n}^{+} - e^{i\alpha L}c_n^{-}(\alpha)}{\alpha^2+\Gamma_n^2}\sin\dfrac{n\pi}{2b}(x+b) & \text{for } |x| < b. \end{cases} \tag{35}$$

Equation (35) is the desired scattered field representation in the Fourier transform domain and holds in the strip $|\tau| < k_2\cos\theta_0$.

4. Simultaneous Wiener-Hopf Equations

Differentiating the field representation for $x > b$ and $x < -b$ in (35) with respect to x and setting $x = \pm b \pm 0$, we find that

$$\Phi'(b+0,\alpha) = -\gamma\Psi(b,\alpha), \tag{36a}$$

$$\Phi'(-b-0,\alpha) = \gamma\Psi(-b,\alpha), \tag{36b}$$

where the prime denotes differentiation with respect to x. We also differentiate the field representation for $|x| < b$ in (35) with respect to x and set $x = \pm b \mp 0$ in the result. This leads to

$$\Phi'(b-0,\alpha) = \Psi(b,\alpha)\gamma\coth 2\gamma b - \Psi(-b,\alpha)\gamma\,\mathrm{csch}2\gamma b + \frac{1}{b}\sum_{n=1}^{\infty}(-)^n\frac{n\pi}{2b}\frac{e^{-i\alpha L}f_{1n}^{-} - e^{i\alpha L}c_n^{+}(\alpha)}{\alpha^2+\gamma_n^2}$$

$$- \frac{1}{b} \sum_{n=1}^{\infty} (-)^n \frac{n\pi}{2b} \frac{e^{-i\alpha L} f_{1n}^{+} - e^{i\alpha L} c_n^{-}(\alpha)}{\alpha^2 + \Gamma_n^2}, \quad (37a)$$

$$\Phi'(-b+0,\alpha) = \Psi(b,\alpha)\gamma \operatorname{csch} 2\gamma b - \Psi(-b,\alpha)\gamma \coth 2\gamma b + \frac{1}{b} \sum_{n=1}^{\infty} \frac{n\pi}{2b} \frac{e^{-i\alpha L} f_{1n}^{-} - e^{i\alpha L} c_n^{+}(\alpha)}{\alpha^2 + \gamma_n^2} - \frac{1}{b} \sum_{n=1}^{\infty} \frac{n\pi}{2b} \frac{e^{-i\alpha L} f_{1n}^{+} - e^{i\alpha L} c_n^{-}(\alpha)}{\alpha^2 + \Gamma_n^2}. \quad (37b)$$

It follows from boundary conditions for tangential magnetic fields across $x = \pm b$ that

$$\Phi'_{-}(\pm b + 0, \alpha) = \Phi'_{-}(\pm b - 0, \alpha), \quad (38a)$$

$$\Phi'_{+}(\pm b + 0, \alpha) = \Phi'_{+}(\pm b - 0, \alpha). \quad (38b)$$

Therefore, subtracting (37 *a*) and (37 *b*) from (36 *a*) and (36 *b*), respectively and taking the sum and difference of the resultant equations, we obtain, after some arrangements, that

$$J_1^d(\alpha) = -\frac{e^{-i\alpha L} U_{-}(\alpha) + e^{i\alpha L} U_{(+)}(\alpha)}{M(\alpha)} + \frac{2}{b} \sum_{n=1,\text{odd}}^{\infty} \frac{n\pi}{2b} \frac{e^{-i\alpha L} f_{1n}^{-} - e^{i\alpha L} c_n^{+}(\alpha)}{\alpha^2 + \gamma_n^2} - \frac{2}{b} \sum_{n=1,\text{odd}}^{\infty} \frac{n\pi}{2b} \frac{e^{-i\alpha L} f_{1n}^{+} - e^{i\alpha L} c_n^{-}(\alpha)}{\alpha^2 + \Gamma_n^2}, \quad (39)$$

$$J_1^s(\alpha) = -\frac{e^{-i\alpha L} V_{-}(\alpha) + e^{i\alpha L} V_{(+)}(\alpha)}{N(\alpha)} - \frac{2}{b} \sum_{n=2,\text{even}}^{\infty} \frac{n\pi}{2b} \frac{e^{-i\alpha L} f_{1n}^{-} - e^{i\alpha L} c_n^{+}(\alpha)}{\alpha^2 + \gamma_n^2} + \frac{2}{b} \sum_{n=2,\text{even}}^{\infty} \frac{n\pi}{2b} \frac{e^{-i\alpha L} f_{1n}^{+} - e^{i\alpha L} c_n^{-}(\alpha)}{\alpha^2 + \Gamma_n^2} \quad (40)$$

with $\operatorname{Re}\nu > 0$, $\operatorname{Re}\nu' > 0$, and

$$\nu_\mu = \frac{1}{\pi}\cos^{-1}\frac{\mu_r - 1}{2(\mu_r + 1)}, \qquad \nu_\varepsilon = \frac{1}{\pi}\cos^{-1}\frac{1 - \varepsilon_r}{2(1 + \varepsilon_r)}, \tag{54}$$

$$\eta(a,b) = \begin{cases} a & \text{for } \operatorname{Re}a \le \operatorname{Re}b, \\ b & \text{for } \operatorname{Re}a \ge \operatorname{Re}b. \end{cases} \tag{55}$$

In (54), the inverse cosine functions are to be interpreted as the principal value. Applying fundamental theorems on the asymptotic behavior of the Fourier integrals [20, 21], we can show with the aid of (9 *a*), (12 *a*, *b*), (13), and (51) that $\Psi_-(\pm b, \alpha)$ and $\Psi_{(+)}(\pm b, \alpha)$ have the asymptotic behavior

$$\Psi_-(\pm b, \alpha) = O(\alpha^{-5/3}) \qquad \text{for } \tau < k_2\cos\theta_0, \tag{56a}$$

$$\Psi_{(+)}(\pm b, \alpha) = O(\alpha^{-1-\nu}) \qquad \text{for } \tau > -k_2\cos\theta_0 \tag{56b}$$

as $\alpha \to \infty$. Similarly, it follows from (9 *b*), (44), and (52) that

$$e^{-i\alpha L}J_1(\pm b, \alpha) = O(\alpha^{-\nu'}) \qquad \text{for } \tau < 0, \tag{57a}$$

$$e^{i\alpha L}J_1(\pm b, \alpha) = O(\alpha^{-2/3}) \qquad \text{for } \tau > 0 \tag{57b}$$

as $\alpha \to \infty$. Therefore, applying (56 *a*, *b*) and (57 *a*, *b*) to (41 *a*, *b*), (42 *a*, *b*), and (43 *a*, *b*), we see that

$$U_-(\alpha), V_-(\alpha) = O(\alpha^{-5/3}) \qquad \text{for } \tau < k_2\cos\theta_0, \tag{58a}$$

$$U_{(+)}(\alpha), V_{(+)}(\alpha) = O(\alpha^{-1-\nu}) \qquad \text{for } \tau > -k_2\cos\theta_0, \tag{58b}$$

$$e^{-i\alpha L}J_1^{d,s}(\alpha) = O(\alpha^{-\nu'}) \qquad \text{for } \tau < 0, \tag{59a}$$

$$e^{i\alpha L}J_1^{d,s}(\alpha) = O(\alpha^{-2/3}) \qquad \text{for } \tau > 0 \tag{59b}$$

as $\alpha \to \infty$. Taking into account (58 *a*, *b*) and (59 *b*) together with (48), it is found that the left-hand and right-hand sides of (50) are $o(1)$ as $\alpha \to \infty$ with $\tau > -k_2\cos\theta_0$ and $\tau < k_2\cos\theta_0$, respectively. These considerations show by application of Liouville's theorem that the entire function $P(\alpha)$ derived before must be identically zero. Equating

the right-hand side of (50) to zero, we obtain that

$$\frac{U_-(\alpha)}{M_-(\alpha)} - \frac{1}{2\pi i}\int_{C_2} \frac{e^{2i\beta L}U_{(+)}(\beta)}{M_-(\beta)(\beta-\alpha)}d\beta - \sum_{n=1,\text{odd}}^{\infty} \frac{n\pi}{b^2}\frac{M_+(i\gamma_n)[f_{1n}^- - e^{-2\gamma_n L}c_n^+(i\gamma_n)]}{2i\gamma_n(\alpha - i\gamma_n)} + \sum_{n=1,\text{odd}}^{\infty} \frac{n\pi}{b^2}\frac{M_+(i\Gamma_n)[f_{1n}^+ - e^{-2\Gamma_n L}c_n^-(i\Gamma_n)]}{2i\Gamma_n(\alpha - i\Gamma_n)} = 0. \quad (60)$$

Next multiplying both sides of (39) by $e^{-i\alpha L}M_-(\alpha)$ and following a procedure similar to that employed above, with the aid of (58 a, b) and (59 a), yields

$$\frac{U_{(+)}(\alpha)}{M_+(\alpha)} + \frac{2B\cos(kb\sin\theta_0)}{M_+(k\cos\theta_0)(\alpha - k\cos\theta_0)} + \frac{1}{2\pi i}\int_{C_1} \frac{e^{-2i\beta L}U_-(\beta)}{M_+(\beta)(\beta-\alpha)}d\beta + \sum_{n=1,\text{odd}}^{\infty} \frac{n\pi}{b^2}\frac{M_+(i\gamma_n)[e^{-2\gamma_n L}f_{1n}^- - c_n^+(-i\gamma_n)]}{2i\gamma_n(\alpha + i\gamma_n)} - \sum_{n=1,\text{odd}}^{\infty} \frac{n\pi}{b^2}\frac{M_+(i\Gamma_n)[e^{-2\Gamma_n L}f_{1n}^+ - c_n^-(-i\Gamma_n)]}{2i\Gamma_n(\alpha + i\Gamma_n)} = 0, \quad (61)$$

where the second term on the left-hand side has appeared in order to cancel a simple pole of $U_{(+)}(\alpha)$ at $\alpha = k\cos\theta_0$.

A similar procedure can also be applied for decomposition of (40). We multiply both sides of (40) by $e^{\pm i\alpha L}N_\pm(\alpha)$ and decompose the resultant equations by making use of (48), (58 a, b), and (59 a, b). Omitting the details, we arrive at

$$\frac{V_-(\alpha)}{N_-(\alpha)} - \frac{1}{2\pi i}\int_{C_2} \frac{e^{2i\beta L}V_{(+)}(\beta)}{N_-(\beta)(\beta-\alpha)}d\beta + \sum_{n=2,\text{even}}^{\infty} \frac{n\pi}{b^2}\frac{N_+(i\gamma_n)[f_{1n}^- - e^{-2\gamma_n L}c_n^+(i\gamma_n)]}{2i\gamma_n(\alpha - i\gamma_n)} - \sum_{n=2,\text{even}}^{\infty} \frac{n\pi}{b^2}\frac{N_+(i\Gamma_n)[f_{1n}^+ - e^{-2\Gamma_n L}c_n^-(i\Gamma_n)]}{2i\Gamma_n(\alpha - i\Gamma_n)} = 0, \quad (62)$$

$$\frac{V_{(+)}(\alpha)}{N_+(\alpha)} - \frac{2iB\sin(kb\sin\theta_0)}{N_+(k\cos\theta_0)(\alpha - k\cos\theta_0)} + \frac{1}{2\pi i}\int_{C_1} \frac{e^{-2i\beta L}V_-(\beta)}{N_+(\beta)(\beta-\alpha)}d\beta$$
$$- \sum_{n=2,\text{even}}^{\infty} \frac{n\pi}{b^2}\frac{N_+(i\gamma_n)[e^{-2\gamma_n L}f_{1n}^- - c_n^+(-i\gamma_n)]}{2i\gamma_n(\alpha+i\gamma_n)}$$
$$+ \sum_{n=2,\text{even}}^{\infty} \frac{n\pi}{b^2}\frac{N_+(i\Gamma_n)[e^{-2\Gamma_n L}f_{1n}^+ - c_n^-(-i\Gamma_n)]}{2i\Gamma_n(\alpha+i\Gamma_n)} = 0. \qquad (63)$$

Equations (60)–(63) are simultaneous integral equations satisfied by the unknown functions $U_-(\alpha), U_{(+)}(\alpha), V_-(\alpha)$, and $V_{(+)}(\alpha)$, where the unknown Fourier coefficients $f_{1n}^{\pm}, f_{2n}$, and g_n are also contained.

6. Some Properties of the Fourier Coefficients

In this section, we shall investigate an important relationship between the unknown Fourier coefficients and the unknown spectral functions. As has already been shown, $\Psi_-(x,\alpha)$ is regular in $\tau < k_2\cos\theta_0$ and $\Psi_{(+)}(x,\alpha)$ is regular in $\tau > -k_2\cos\theta_0$ except for a simple pole at $\alpha = k\cos\theta_0$, whereas $\Phi_1(x,\alpha)$ is an entire function. From these considerations, it follows that

$$\lim_{\alpha\to -i\gamma_n}(\alpha+i\gamma_n)\Psi_-(x,\alpha) = 0, \qquad (64a)$$

$$\lim_{\alpha\to i\gamma_n}(\alpha-i\gamma_n)\Psi_{(+)}(x,\alpha) = 0, \qquad (64b)$$

$$\lim_{\alpha\to \pm i\Gamma_n}(\alpha\mp i\Gamma_n)\Phi_1(x,\alpha) = 0 \qquad (64c)$$

for $n = 1, 2, 3, \cdots$. Substituting (30), (32), and (33) into (64 *a*), (64 *b*), and (64 *c*), respectively, we derive, after some manipulations, that

$$f_{1n}^- = \begin{cases} -(n\pi/2b)U_-(-i\gamma_n) & \text{for odd } n, \\ (n\pi/2b)V_-(-i\gamma_n) & \text{for even } n, \end{cases} \qquad (65)$$

$$c_n^+(i\gamma_n) = \begin{cases} (n\pi/2b)U_{(+)}(i\gamma_n) & \text{for odd } n, \\ -(n\pi/2b)V_{(+)}(i\gamma_n) & \text{for even } n, \end{cases} \qquad (66)$$

$$f_{1n}^{+} - e^{-2\Gamma_n L} c_n^{-}(i\Gamma_n) = 0 \quad \text{for } n = 1, 2, 3, \cdots, \tag{67a}$$

$$e^{-2\Gamma_n L} f_{1n}^{+} - c_n^{-}(-i\Gamma_n) = 0 \quad \text{for } n = 1, 2, 3, \cdots. \tag{67b}$$

Equations (66) and (67 a, b) constitute a system of algebraic equations, which relates the Fourier coefficients f_{1n}^{+}, f_{2n}, and g_n with the functions $U_{(+)}(\alpha)$ and $V_{(+)}(\alpha)$. Solving these equations for f_{1n}^{+}, f_{2n}, and g_n, we are led to

$$f_{1n}^{+} = \begin{cases} (n\pi/2b) P_n U_{(+)}(i\gamma_n) & \text{for odd } n, \\ -(n\pi/2b) P_n V_{(+)}(i\gamma_n) & \text{for even } n, \end{cases} \tag{68a}$$

$$f_{2n} = \begin{cases} (n\pi/2b) Q_n U_{(+)}(i\gamma_n) & \text{for odd } n, \\ -(n\pi/2b) Q_n V_{(+)}(i\gamma_n) & \text{for even } n, \end{cases} \tag{68b}$$

$$g_n = \begin{cases} (n\pi/2b) R_n U_{(+)}(i\gamma_n) & \text{for odd } n, \\ -(n\pi/2b) R_n V_{(+)}(i\gamma_n) & \text{for even } n, \end{cases} \tag{68c}$$

where

$$P_n = \frac{2\mu_r \Gamma_n}{\mu_r \gamma_n + \Gamma_n} \frac{e^{-2\Gamma_n L}}{1 - \rho_n e^{-4\Gamma_n L}}, \tag{69a}$$

$$Q_n = \frac{\mu_r \Gamma_n}{\mu_r \gamma_n + \Gamma_n} \frac{1 + e^{-4\Gamma_n L}}{1 - \rho_n e^{-4\Gamma_n L}}, \tag{69b}$$

$$R_n = \frac{\mu_r}{\mu_r \gamma_n + \Gamma_n} \frac{1 - e^{-4\Gamma_n L}}{1 - \rho_n e^{-4\Gamma_n L}}, \tag{69c}$$

$$\rho_n = (\mu_r \gamma_n - \Gamma_n)/(\mu_r \gamma_n + \Gamma_n). \tag{70}$$

Substituting (68 b, c) into the first equation of (34) and setting $\alpha = -i\gamma_n$, we also find that

$$c_n^{+}(-i\gamma_n) = \begin{cases} (n\pi/2b) \kappa_n U_{(+)}(i\gamma_n) & \text{for odd } n, \\ -(n\pi/2b) \kappa_n V_{(+)}(i\gamma_n) & \text{for even } n, \end{cases} \tag{71}$$

where

$$\kappa_n = \frac{e^{-4\Gamma_n L} - \rho_n}{1 - \rho_n e^{-4\Gamma_n L}}. \tag{72}$$

Equations (65), (66), (67 a, b), and (71) can be conveniently used in simplifying the integral equations (60)–(63).

7. Formal Solution

Let us define the integral in (60) as

$$I = \frac{1}{2\pi i} \int_{C_2} \frac{e^{2i\beta L} U_{(+)}(\beta)}{M_-(\beta)(\beta - \alpha)} d\beta. \tag{73}$$

It is seen from (12 b), (41 b), (46 a), and (47 a) that singularities of the integrand of I in $\mathrm{Im}\beta > c$ (see Fig. 2) are simple poles at $\beta = k\cos\theta_0$ and $i\gamma_n$ with $n = 1, 3, 5, \cdots$ and a branch point at $\beta = k$. We choose a branch cut emanating from $\beta = k$ as a straight line that is parallel to the imaginary axis and goes to infinity in the upper half-plane. Then I is evaluated by deforming the contour into the upper half-plane with the following result:

$$I = J_u^{(1)}(\alpha) + \frac{2A\cos(kb\sin\theta_0)}{M_-(k\cos\theta_0)(\alpha - k\cos\theta_0)} + \sum_{n=1,\mathrm{odd}}^{\infty} \left(\frac{n\pi}{2b}\right)^2 \frac{e^{-2\gamma_n L} M_+(i\gamma_n) U_{(+)}(i\gamma_n)}{bi\gamma_n(\alpha - i\gamma_n)}, \tag{74}$$

where

$$J_u^{(1)}(\alpha) = \frac{1}{2\pi i} \int_C \frac{e^{2i\beta L} U_{(+)}(\beta)}{M_-(\beta)(\beta - \alpha)} d\beta. \tag{75}$$

In (75), C is the contour composed of two straight paths $C_\pm$ along the branch cut and a portion C_ε of a circle with radius $\varepsilon(\ll 1)$, centered at the branch point $\beta = k$, as shown in Fig. 3. The integral $J_u^{(1)}(\alpha)$ is now reduced to

$$J_u^{(1)}(\alpha) = \frac{1}{\pi i} \int_k^{k+i\infty} e^{2i\beta L} \frac{(\beta^2 - k^2)^{1/2} M_+(\beta) U_{(+)}(\beta)}{\beta - \alpha} d\beta \tag{76}$$

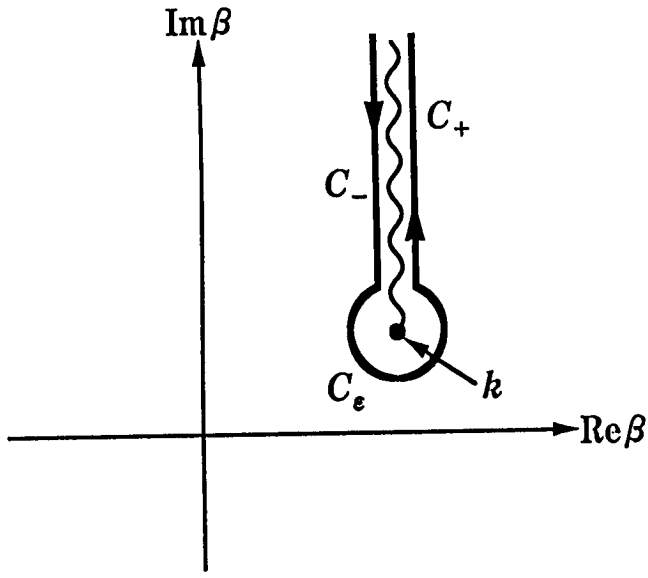

Figure 3. Integration path $C(\equiv C_- + C_\varepsilon + C_+)$ for $J_u^{(1)}(\alpha)$ defined by (75).

by letting the radius ε of C_ε tend to zero and combining the resultant contributions from $C_\pm$, where the contour is the one running parallel to the imaginary axis on the right-hand side of the branch cut. Substituting (74) into (60) and taking into account (65), (66), and (67 *a*), we derive that

$$\frac{U_-(\alpha)}{b} = \frac{M_-(\alpha)}{b^{1/2}}\left[\frac{A_u}{b(\alpha - k\cos\theta_0)} + \frac{J_u^{(1)}(\alpha)}{b^{1/2}} - \sum_{n=2}^{\infty}\frac{a_n p_n u_n^-}{b(\alpha - i\gamma_{2n-3})}\right] \tag{77}$$

for $\alpha \neq k, k\cos\theta_0$, where $J_u^{(1)}(\alpha)$ is given by (76), and

$$a_n = \frac{[(n-3/2)\pi]^2}{bi\gamma_{2n-3}}, \qquad p_n = \frac{M_+(i\gamma_{2n-3})}{b^{1/2}}, \tag{78}$$

$$u_n^- = \frac{U_-(-i\gamma_{2n-3})}{b}, \qquad A_u = \frac{2b^{1/2}A\cos(kb\sin\theta_0)}{M_-(k\cos\theta_0)}. \tag{79}$$

We next evaluate the integral involved in (61) by following a procedure similar to that employed to obtain (74) and (76), and simplify the result

with the aid of (65), (67 *b*), and (71). This leads to

$$\frac{U_{(+)}(\alpha)}{b} = \frac{M_+(\alpha)}{b^{1/2}}\left[-\frac{B_u}{b(\alpha - k\cos\theta_0)} + \frac{J_u^{(2)}(\alpha)}{b^{1/2}} + \sum_{n=2}^{\infty}\frac{\kappa_{2n-3}a_n p_n u_n^+}{b(\alpha + i\gamma_{2n-3})}\right] \tag{80}$$

for $\alpha \neq -k, k\cos\theta_0$, where

$$u_n^+ = \frac{U_{(+)}(i\gamma_{2n-3})}{b}, \qquad B_u = \frac{2b^{1/2}B\cos(kb\sin\theta_0)}{M_+(k\cos\theta_0)}, \tag{81}$$

$$J_u^{(2)}(\alpha) = \frac{1}{\pi i}\int_k^{k+i\infty} e^{2i\beta L}\frac{(\beta^2 - k^2)^{1/2}M_+(\beta)U_-(-\beta)}{\beta + \alpha}d\beta\,. \tag{82}$$

A similar procedure can also be applied to (62) and (63), and we finally arrive at

$$\frac{V_-(\alpha)}{b} = \frac{N_-(\alpha)}{b^{1/2}}\left[-\frac{A_v}{b(\alpha - k\cos\theta_0)} + \frac{J_v^{(1)}(\alpha)}{b^{1/2}} - \sum_{n=2}^{\infty}\frac{b_n q_n v_n^-}{b(\alpha - i\gamma_{2n-2})}\right] \tag{83}$$

for $\alpha \neq k, k\cos\theta_0$, and

$$\frac{V_{(+)}(\alpha)}{b} = \frac{N_+(\alpha)}{b^{1/2}}\left[\frac{B_v}{b(\alpha - k\cos\theta_0)} + \frac{J_v^{(2)}(\alpha)}{b^{1/2}} + \sum_{n=2}^{\infty}\frac{\kappa_{2n-2}b_n q_n v_n^+}{b(\alpha + i\gamma_{2n-2})}\right] \tag{84}$$

for $\alpha \neq -k, k\cos\theta_0$, where

$$b_n = \frac{[(n-1)\pi]^2}{bi\gamma_{2n-2}}, \qquad q_n = \frac{N_+(i\gamma_{2n-2})}{b^{1/2}}, \tag{85}$$

$$v_n^- = \frac{V_-(-i\gamma_{2n-2})}{b}, \qquad A_v = \frac{2ib^{1/2}A\sin(kb\sin\theta_0)}{N_-(k\cos\theta_0)}, \tag{86a}$$

$$v_n^+ = \frac{V_{(+)}(i\gamma_{2n-2})}{b}, \qquad B_v = \frac{2ib^{1/2}B\sin(kb\sin\theta_0)}{N_+(k\cos\theta_0)}, \tag{86b}$$

$$J_v^{(1)}(\alpha) = \frac{1}{\pi i}\int_k^{k+i\infty} e^{2i\beta L}\frac{(\beta^2-k^2)^{1/2}N_+(\beta)V_{(+)}(\beta)}{\beta-\alpha}d\beta, \tag{87a}$$

$$J_v^{(2)}(\alpha) = \frac{1}{\pi i}\int_k^{k+i\infty} e^{2i\beta L}\frac{(\beta^2-k^2)^{1/2}N_+(\beta)V_-(-\beta)}{\beta+\alpha}d\beta. \tag{87b}$$

Equations (77), (80), (83), and (84) give the formal solution to the simultaneous Wiener-Hopf equations (39) and (40). We should note that the formal solution involves the infinite series with the unknowns $u_n^{\pm}$ and $v_n^{\pm}$ for $n = 2, 3, 4\cdots$ as well as the branch-cut integrals $J_u^{(1)}(\alpha), J_u^{(2)}(\alpha), J_v^{(1)}(\alpha)$, and $J_v^{(2)}(\alpha)$ with unknown integrands. It is therefore required to develop approximation procedures for the explicit solution.

8. Approximate Solution

In this section, we shall discuss efficient methods for approximate evaluation of the infinite series and the branch-cut integrals occurring in (77), (80), (83), and (84) to derive the approximate solution of the Wiener-Hopf equations. Similar infinite series and branch-cut integrals appear in the formal solution to the diffraction problem involving the cavity with no material loading, and the method of evaluation has been discussed in detail by the authors in the previous papers [22, 23]. Since the approximate solution to the present problem can be deduced by following a procedure similar to that developed in our previous papers, we shall give only the final results after brief explanation of the method.

First let us consider approximation of the infinite series contained in (77), (80), (83), and (84). Using (58 a, b), we deduce from (79), (81), and (86 a, b) that

$$u_n^- \sim 2^{1/2}K_u^{(1)}(b\gamma_{2n-3})^{-5/3}, \quad u_n^+ \sim 2^{1/2}K_u^{(2)}(b\gamma_{2n-3})^{-1-\nu}, \tag{88a}$$

$$v_n^- \sim 2^{1/2} K_v^{(1)} (b\gamma_{2n-2})^{-5/3}, \quad v_n^+ \sim 2^{1/2} K_u^{(2)} (b\gamma_{2n-2})^{-1-\nu} \tag{88b}$$

as $n \to \infty$, where $K_u^{(1)}, K_u^{(2)}, K_v^{(1)}$, and $K_v^{(2)}$ are unknown constants. Taking a large positive integer N, the unknowns $u_n^{\pm}$ and $v_n^{\pm}$ for $n \geq N$ of the infinite series in (77), (80), (83), and (84) may be approximated by the asymptotic behavior given in (88 a, b) with reasonable accuracy. Then we can replace each infinite series in (77), (80), (83), and (84) approximately by the sum of the finite series containing $N-2$ unknowns and the residual infinite series with one unknown constant. This procedure yields accurate approximate expressions for the original infinite series since the edge condition is taken into account explicitly.

On the other hand, we have provided in Appendix a fundamental theorem [23, 26] for asymptotic evaluation of certain branch-cut integrals arising frequently in the Wiener-Hopf analysis. Now it is seen that the branch-cut integrals defined by (76), (82), and (87 a, b) can be reduced to the canonical form as given by ($A.1$). Therefore, we can apply Theorem in Appendix to derive asymptotic expansions of these branch-cut integrals for large $|k|L$. Keeping only the leading terms from the asymptotic series and carrying out some manipulations with the aid of (88 a, b), we finally arrive at the approximate expressions of (77), (80), (83), and (84) as follows:

$$\begin{aligned}\frac{U_-(\alpha)}{b} \approx \frac{M_-(\alpha)}{b^{1/2}} \Bigg(& \frac{A_u}{b(\alpha - k\cos\theta_0)} \\ & + a_1 p_1 \Bigg\{ \left[u_1^+ + \frac{2B\cos(kb\sin\theta_0)}{kb(1-\cos\theta_0)} \right] \xi(-\alpha) \\ & + \frac{2LB}{b} \cos(kb\sin\theta_0) \chi(-\alpha, -k\cos\theta_0) \Bigg\} \\ & - \sum_{n=2}^{N-1} \frac{a_n p_n u_n^-}{b(\alpha - i\gamma_{2n-3})} - K_u^{(1)} S_{uN}^{(1)}(\alpha) \Bigg), \end{aligned} \tag{89a}$$

$$\frac{U_{(+)}(\alpha)}{b} \approx \frac{M_+(\alpha)}{b^{1/2}} \left(- \frac{B_u}{b(\alpha - k\cos\theta_0)} \right.$$

$$+ a_1 p_1 \left\{ \left[u_1^- + \frac{2A\cos(kb\sin\theta_0)}{kb(1+\cos\theta_0)} \right] \xi(\alpha) + \frac{2LA}{b}\cos(kb\sin\theta_0)\chi(\alpha, k\cos\theta_0) \right\} + \sum_{n=2}^{N-1} \frac{\kappa_{2n-3} a_n p_n u_n^+}{b(\alpha + i\gamma_{2n-3})} + K_u^{(2)} S_{uN}^{(2)}(\alpha) \Bigg), \tag{89b}$$

$$\frac{V_-(\alpha)}{b} \approx \frac{N_-(\alpha)}{b^{1/2}} \Bigg(- \frac{A_v}{b(\alpha - k\cos\theta_0)} + b_1 q_1 \left\{ \left[v_1^+ - \frac{2iB\sin(kb\sin\theta_0)}{kb(1-\cos\theta_0)} \right] \xi(-\alpha) - \frac{2iLB}{b}\sin(kb\sin\theta_0)\chi(-\alpha, -k\cos\theta_0) \right\} - \sum_{n=2}^{N-1} \frac{b_n q_n v_n^-}{b(\alpha - i\gamma_{2n-2})} - K_u^{(1)} S_{uN}^{(1)}(\alpha) \Bigg), \tag{90a}$$

$$\frac{V_{(+)}(\alpha)}{b} \approx \frac{N_+(\alpha)}{b^{1/2}} \Bigg(\frac{B_v}{b(\alpha - k\cos\theta_0)} + b_1 q_1 \left\{ \left[v_1^- + \frac{2iA\sin(kb\sin\theta_0)}{kb(1+\cos\theta_0)} \right] \xi(\alpha) - \frac{2iLA}{b}\sin(kb\sin\theta_0)\chi(\alpha, k\cos\theta_0) \right\} + \sum_{n=2}^{N-1} \frac{\kappa_{2n-2} b_n q_n v_n^+}{b(\alpha + i\gamma_{2n-2})} + K_v^{(2)} S_{vN}^{(2)}(\alpha) \Bigg), \tag{90b}$$

where

$$a_1 = kb, \qquad b_1 = kb, \tag{91}$$

$$p_1 = \frac{M_+(k)}{b^{1/2}}, \qquad q_1 = \frac{N_+(k)}{b^{1/2}}, \tag{92}$$

$$u_1^- = \frac{U_-(-k)}{b}, \qquad u_1^+ = \frac{U_{(+)}(k)}{b}, \tag{93a}$$

$$v_1^- = \frac{V_-(-k)}{b}, \qquad v_1^+ = \frac{V_{(+)}(k)}{b}, \tag{93b}$$

$$\xi(\alpha) = \frac{e^{i(2kL-\pi/4)}}{\pi(kL)^{1/2}}\Gamma_1[3/2, -2i(\alpha+k)L], \tag{94}$$

$$\chi(\alpha,\beta) = \frac{\xi(\alpha)-\xi(\beta)}{(\alpha-\beta)L}, \tag{95}$$

$$S_{uN}^{(1)}(\alpha) = \sum_{n=N}^{\infty} \frac{a_n(b\gamma_{2n-3})^{-13/6}}{b(\alpha - i\gamma_{2n-3})}, \tag{96a}$$

$$S_{uN}^{(2)}(\alpha) = \sum_{n=N}^{\infty} \frac{\kappa_{2n-3}a_n(b\gamma_{2n-3})^{-3/2-\nu}}{b(\alpha + i\gamma_{2n-3})}, \tag{96b}$$

$$S_{vN}^{(1)}(\alpha) = \sum_{n=N}^{\infty} \frac{b_n(b\gamma_{2n-2})^{-13/6}}{b(\alpha - i\gamma_{2n-2})}, \tag{97a}$$

$$S_{vN}^{(2)}(\alpha) = \sum_{n=N}^{\infty} \frac{\kappa_{2n-2}b_n(b\gamma_{2n-2})^{-3/2-\nu}}{b(\alpha + i\gamma_{2n-2})}. \tag{97b}$$

In (94), $\Gamma_1(\cdot,\cdot)$ is the generalized gamma function [23, 27] defined by

$$\Gamma_m(u,v) = \int_0^\infty \frac{t^{u-1}e^{-t}}{(t+v)^m}\,dt \tag{98}$$

for Re $u > 0$, $|v| > 0$, $|\arg v| < \pi$, and positive integer m.

Equations (89 a, b) and (90 a, b) give the approximate solution to the simultaneous Wiener-Hopf equations (39) and (40), and they hold uniformly in θ_0 for large N and $|k|L$, where the unknowns $u_n^{\pm}$ and $v_n^{\pm}$ for $n = 1, 2, 3, \cdots, N-1$ as well as $K_u^{(1)}, K_u^{(2)}, K_v^{(1)}$, and $K_v^{(2)}$ are contained. In order to determine these unknowns, we set $\alpha = -k, -i\gamma_{2m-3}$ and $\alpha = k, i\gamma_{2m-3}$ for $m = 2, 3, 4, \cdots, N$ in (89 a) and (89 b), respectively. We also set $\alpha = -k, -i\gamma_{2m-2}$ and

$\alpha = k, i\gamma_{2m-2}$ for $m = 2, 3, 4, \cdots, N$ in (90 a) and (90 b), respectively. These procedures lead to the two sets of $2N$ equations, where $u_N^{\pm}$ and $v_N^{\pm}$ are involved. Since N is a large positive integer, we can employ (88 a, b) to replace $u_N^{\pm}$ and $v_N^{\pm}$ by their asymptotic behavior containing $K_u^{(1)}, K_u^{(2)}, K_v^{(1)}$, and $K_v^{(2)}$. Thus, the two sets of $2N \times 2N$ matrix equations are derived, which can be solved numerically with high accuracy. In the above discussions, we have derived only the leading terms of asymptotic expansions for the branch-cut integrals, but their complete asymptotic series including all the higher order terms may also be explicitly derived by applying the method developed recently by the authors [28]. The approximation procedures developed in this section are based on rigorous asymptotics with the aid of the edge condition and hence, the above approximate solution is valid over a wide frequency range as long as the cavity depth $2L$ is not too small compared with the wavelength.

9. Scattered Field

The scattered field in the real space is obtained by taking the inverse Fourier transform of (35) according to the formula:

$$\phi(x, z) = (2\pi)^{-1/2} \int_{-\infty+ic}^{\infty+ic} \Phi(x, \alpha) e^{-i\alpha z} d\alpha, \tag{99}$$

where c is a constant such that $|c| < k_2 \cos\theta_0$. First we shall consider the field inside the cavity. Substituting the field expression for $|x| < b$ in (35) to (99), we find that

$$\begin{aligned}
\phi(x, z) =& (2\pi)^{-1/2} \int_{-\infty+ic}^{\infty+ic} \left[\Psi_-(b, \alpha) \frac{\sinh \gamma(x+b)}{\sinh 2\gamma b} \right. \\
& - \Psi_-(-b, \alpha) \frac{\sinh \gamma(x-b)}{\sinh 2\gamma b} \\
& \left. + \frac{1}{b} \sum_{n=1}^{\infty} \left(\frac{f_{1n}^-}{\alpha^2 + \gamma_n^2} - \frac{f_{1n}^+}{\alpha^2 + \Gamma_n^2} \right) \sin \frac{n\pi}{2b}(x+b) \right] e^{-i\alpha(z+L)} d\alpha \\
& + (2\pi)^{-1/2} \int_{-\infty+ic}^{\infty+ic} \left\{ \Psi_{(+)}(b, \alpha) \frac{\sinh \gamma(x+b)}{\sinh 2\gamma b} \right.
\end{aligned}$$

$$- \Psi_{(+)}(-b,\alpha)\frac{\sinh\gamma(x-b)}{\sinh 2\gamma b}$$
$$-\frac{1}{b}\sum_{n=1}^{\infty}\left[\frac{c_n^+(\alpha)}{\alpha^2+\gamma_n^2}-\frac{c_n^-(\alpha)}{\alpha^2+\Gamma_n^2}\right]\sin\frac{n\pi}{2b}(x+b)\Bigg\}e^{-i\alpha(z-L)}d\alpha. \tag{100}$$

Since the region inside the cavity exists for $-L<z<L$, the first and second integrals in (100) can be evaluated by deforming the contour into the lower and upper half-planes, respectively. Taking into account the regularity of $\Psi_-(x,\alpha)$ and $\Psi_{(+)}(x,\alpha)$ together with (30) and (32), it is seen that the integrands of the first and second integrals are regular at $\alpha=-i\gamma_n$ and $i\gamma_n$ for $n=1,2,3,\cdots$, respectively. Therefore, in the process of deformation of the contour, singularities associated with the first integral are simple poles at $\alpha=-i\Gamma_n$ for $n=1,2,3,\cdots$, whereas singularities associated with the second integral are simple poles at $\alpha=k\cos\theta_0$ and $i\Gamma_n$ for $n=1,2,3,\cdots$. Thus, evaluating the integrals by the use of (67a) and (68a) leads to the following result:

$$\phi(x,z)=-e^{-ik(x\sin\theta_0+z\cos\theta_0)}$$
$$+\sum_{n=1}^{\infty}T_n\sin\frac{n\pi}{2b}(x+b)\sinh\Gamma_n(z+L), \tag{101}$$

where

$$T_n=\begin{cases}(\frac{\pi}{2})^{1/2}\dfrac{n\pi}{b^2\Gamma_n}P_nU_{(+)}(i\gamma_n) & \text{for odd } n,\\ -(\frac{\pi}{2})^{1/2}\dfrac{n\pi}{b^2\Gamma_n}P_nV_{(+)}(i\gamma_n) & \text{for even } n.\end{cases} \tag{102}$$

In (101), the first term exactly cancels the incident field defined by (2), as expected, whereas the second term represents the transmitted TE modes coupling into the cavity. It is found by taking into account (81) and (86b) that the transmission coefficients T_{2n-3} and T_{2n-2} for $n=2,3,4,\cdots$ are expressed in terms of u_n^+ and v_n^+, respectively.

Next we shall consider the field outside the cavity and derive the scattered far field based on the saddle point method. Substituting the field expression for $x>b$ and $x<-b$ in (35) to (99), it is found that

$$\phi(x,z)=(2\pi)^{-1/2}\int_{-\infty+ic}^{\infty+ic}\Psi(\pm b,\alpha)e^{\mp\gamma(x\mp b)-i\alpha z}d\alpha \tag{103}$$

for $x \gtrless \pm b$, where $\Psi(\pm b, \alpha)$ is expressed as

$$\Psi(\pm b, \alpha) = e^{-i\alpha L}\frac{U_-(\alpha) \pm V_-(\alpha)}{2} + e^{i\alpha L}\frac{U_{(+)}(\alpha) \pm V_{(+)}(\alpha)}{2} \tag{104}$$

by making use of (11), (41 a, b), and (42 a, b). The field outside the cavity is represented as a combination of (100) with $|z| > L$ and (103), but the contributions from the region $|x| < b$ outside the cavity are negligibly small at large distances from the origin. Therefore, the derivation of the scattered far field for $|x| < b$ will not be discussed in the following. We note that (77) and (83) are regular in α except for a branch point $\alpha = k$ and a simple pole $\alpha = k\cos\theta_0$, whereas (80) and (84) are regular in α except for a branch point $\alpha = -k$ and a simple pole $\alpha = k\cos\theta_0$. Now, by taking into account (77), (80), (83), (84), and (104) together with (13), (79), (81), and (86 a, b), it is verified that $\Psi(\pm b, \alpha)$ given by (104) is regular at $\alpha = k\cos\theta_0$. This shows that singularities of the integrand of (103) are only branch points at $\alpha = \pm k$. Hence, introducing the polar coordinate

$$x = \rho\sin\theta, \qquad z = \rho\cos\theta \qquad \text{for } 0 < |\theta| < \pi \tag{105}$$

and applying the saddle point method, we derive a far field expression of (103) with the result that

$$\phi(\rho, \theta) \sim \pm\Psi(\pm b, -k\cos\theta)\, k\sin\theta e^{\mp ikb\sin\theta}\frac{e^{i(k\rho-\pi/4)}}{(k\rho)^{1/2}} \tag{106}$$

for $x \gtrless \pm b$ as $k\rho \to \infty$. Although (106) has been derived only for the region $|x| > b$ (i.e., $0 < |\theta| < \pi$), it can be shown that (106) is continuous across $|\theta| = 0, \pi$. Therefore, it is essentially not necessary to evaluate (100) for large $|k|\rho$, since (106) is valid for arbitrary θ. The analysis has thus far been carried out by assuming $0 < \theta_0 < \pi/2$, but the results are in fact true for arbitrary θ_0.

10. Numerical Results and Discussion

In this section, we shall show representative numerical examples of the monostatic RCS and the bistatic RCS for various physical parameters to discuss the scattering characteristics of the cavity in detail.

Since the problem considered here is of the two-dimensional scattering, the RCS per unit length (echo width) is defined by

$$\sigma = \lim_{\rho \to \infty} \left(2\pi\rho \frac{|\phi|^2}{|\phi^i|^2} \right). \tag{107}$$

For real k, (107) is simplified using (2) and (106) as

$$\sigma = \lambda \, |\Psi(\pm b, -k\cos\theta)\, k \sin\theta|^2 \tag{108}$$

with $\theta \gtrless 0$, where λ is the free-space wavelength. Numerical results presented here are based on the scattered far field expression given by (106) together with (104). We have used the approximate expressions as derived in $(89\,a,b)$ and $(90\,a,b)$ for computing $U_-(\alpha), U_{(+)}(\alpha)$, $V_-(\alpha)$, and $V_{(+)}(\alpha)$ involved in (104). As has been mentioned at the end of Section 8, we require numerical inversion of the two sets of $2N \times 2N$ matrix equations for obtaining all the physical quantities. A general consideration on the Wiener-Hopf technique shows that the convergence of the approximate solution obtained in Section 8 is very fast when the cavity aperture $2b$ is small and the cavity depth $2L$ is large, compared with the wavelength, particularly because we do not require large N in these circumstances. By careful numerical experimentation on the convergence rate of the approximate solution, we have found that the choice of $N = 5, 10$, and 13 yields sufficient accuracy for cavities with $2b = \lambda, 5\lambda$, and 10λ, respectively.

Figures 4–6 and 7–9 are numerical results of the monostatic RCS versus the incidence angle θ_0 and the bistatic RCS versus the observation angle θ, respectively, where the values of σ/λ have been plotted in decibels [dB] by computing $10\log_{10}\sigma/\lambda$. The cavity structure is symmetric along the z-axis so that we have shown the monostatic RCS only for the range $0° \le \theta_0 \le 180°$, whereas for the bistatic RCS, the incidence angle θ_0 is fixed as $60°$ in all numerical examples. For numerical computations, three different values of the ratio L/b have been taken as 1.0, 2.0, and 3.0, and the ferrite with $\varepsilon_r = 2.5 + i1.25$ and $\mu_r = 1.6 + i0.8$ [4] has been chosen as an example of lossy materials. In order to investigate the scattering mechanism for each L/b over wide frequency range, numerical computations have been carried out for three typical values of the cavity aperture opening, namely, $2b = \lambda, 5\lambda$, and 10λ. The previous results for no material loading [22–24] have also been added by dashed lines to investigate clearly the effect of lossy material loading inside the cavity.

From Figs. 4–6, we observe noticeable peaks at $\theta_0 = 90°$ and $180°$ in all numerical examples, which are due to the specular reflection from the sideplate surface at $x = b + 0$ and the endplate surface at $z = -L - 0$, respectively. For most of the RCS curves in the figures, we also see peaks at $\theta_0 = 0°$ which correspond to the specular reflection from the endplate surface at $z = -L + 0$ for empty cavities and that from the material boundary at $z = L$ for loaded cavities. It is found that the RCS data for fixed $2b$ show sharper peaks at $\theta_0 = 90°$ with an increase of L/b since the length of the sideplate surface at $x = b$ is then increased. From the solid and dashed curves for each fixed L/b and $2b$, we notice that both characteristics over the range $90° \leq \theta_0 \leq 180°$ are nearly identical to each other, not depending on the material inside the cavity. Hence, it is confirmed that, when the cavity aperture is invisible from the source point, main contributions to the backscattered far field arise due to the exterior features of the cavity and the difference on the interior cavity geometries does not affect the backscattering in the far field. On the other hand, by comparing the two RCS curves for each L/b and $2b$ over $0° \leq \theta_0 \leq 90°$, there is obviously a difference depending on the material inside the cavity. Therefore, we see that when the cavity aperture is in the illuminated region against the incident field, the material loading inside the cavity significantly affects the backscattered far field. More explicitly, for empty cavities, the monostatic RCS is smoothly varying and exhibits fairly large values over some range in $0° \leq \theta_0 \leq 90°$ due to the effect of interior irradiation, whereas the irradiation is reduced for the case of material loading. We also find by comparing the results for $2b = \lambda, 5\lambda$, and 10λ that this reduction is noticeable for larger cavities. This shows that, for large cavities, good RCS reduction can be achieved over a wide range of the incidence angle by lossy material loading inside the cavity.

From Figs. 7–9, it is seen that in all numerical examples, the bistatic RCS shows the largest and the second largest values at the incident and reflected shadow boundaries given by $\theta_0 = -120°$ and $120°$ respectively, as expected. The peaks along these two directions

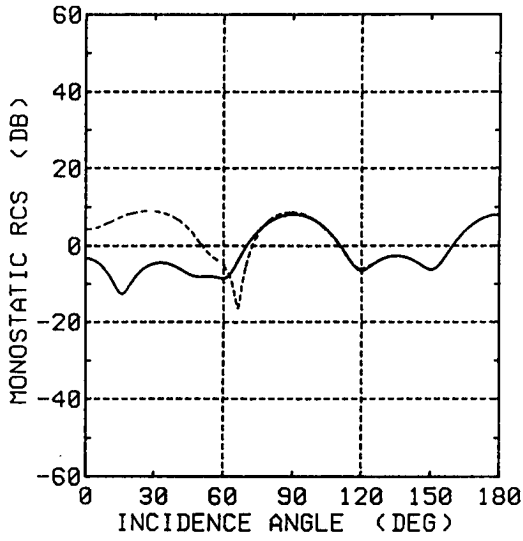

Figure 4a. Monostatic RCS σ/λ [dB] for $L/b = 1.0, 2b = \lambda$. Solid lines and dashed lines denote the results for a material-loaded cavity with $\epsilon_r = 2.5 + i1.25, \mu_r = 1.6 + i0.8$ and an empty cavity, respectively.

become sharper with an increase of the cavity aperture $2b$ for fixed L/b. On comparing the results for empty cavities with those for loaded cavities, the effect of material loading inside the cavity can be seen clearly over the range $|\theta| < 90°$, and the RCS reduction occurs for loaded cavities. This is because, the cavity aperture is then visible from the observation point and the interior features of the cavity affect explicitly the far field bistatic scattering. On the other hand, the bistatic RCS results with and without material loading show close characteristics over the range $110° \leq |\theta| \leq 180°$, since main contributions to the scattered far field are due to the exterior features of the cavity geometry. For larger cavities with no material loading, there are some particular peaks in the neighborhood of $\theta = \pm 60°$, which are caused by the interior irradiation. As has been recognized in our previous papers [22, 23], the direction in which the irradiated fields are strongly excited, in general, depends on the incidence angle for wide cavity apertures. From the results presented in the figures, we see that when the cavity aperture opening is large, the RCS reduction for the loaded case is noticeable around $\theta = 60°$.

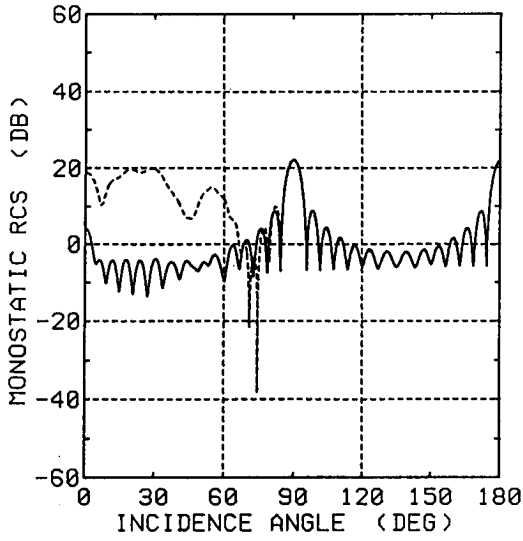

Figure 4b. Monostatic RCS σ/λ [dB] for $L/b = 1.0, 2b = 5\lambda$. Other particulars are the same as in Fig. 4a.

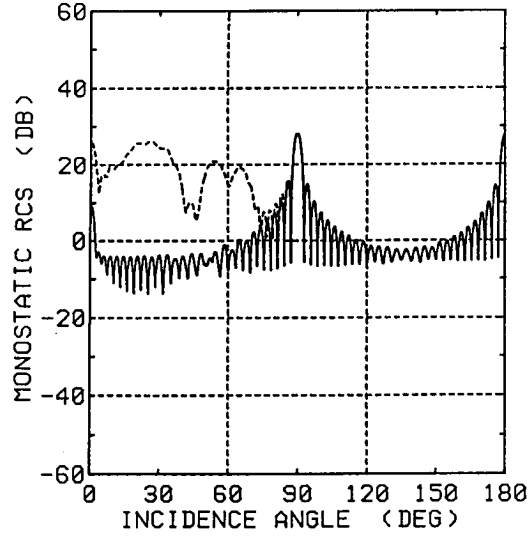

Figure 4c. Monostatic RCS σ/λ [dB] for $L/b = 1.0, 2b = 10\lambda$. Other particulars are the same as in Fig. 4a.

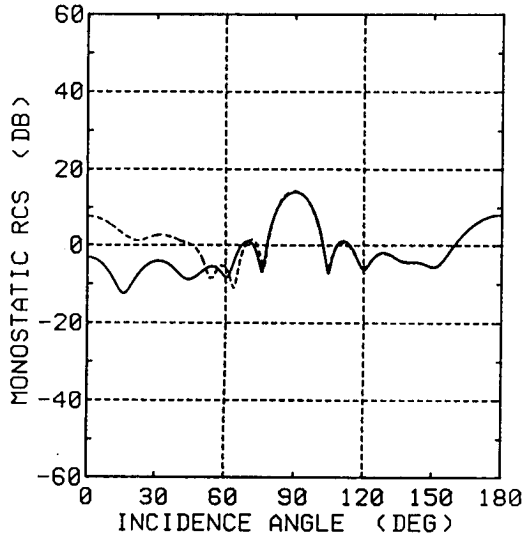

Figure 5a. Monostatic RCS σ/λ [dB] for $L/b = 2.0, 2b = \lambda$. Other particulars are the same as in Fig. 4a.

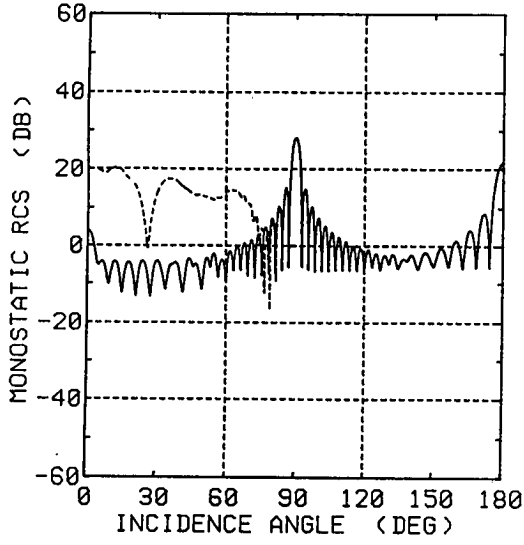

Figure 5b. Monostatic RCS σ/λ [dB] for $L/b = 2.0, 2b = 5\lambda$. Other particulars are the same as in Fig. 4a.

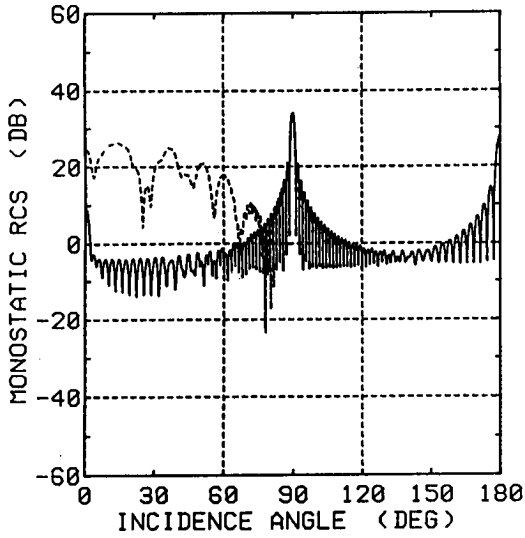

Figure 5c. Monostatic RCS σ/λ [dB] for $L/b = 2.0, 2b = 10\lambda$. Other particulars are the same as in Fig. 4a.

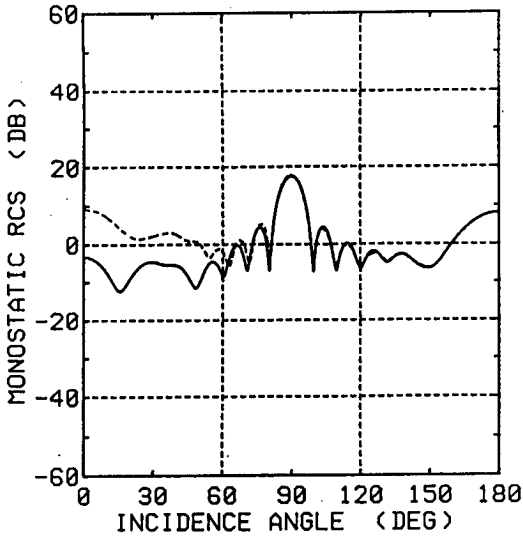

Figure 6a. Monostatic RCS σ/λ [dB] for $L/b = 3.0, 2b = \lambda$. Other particulars are the same as in Fig. 4a.

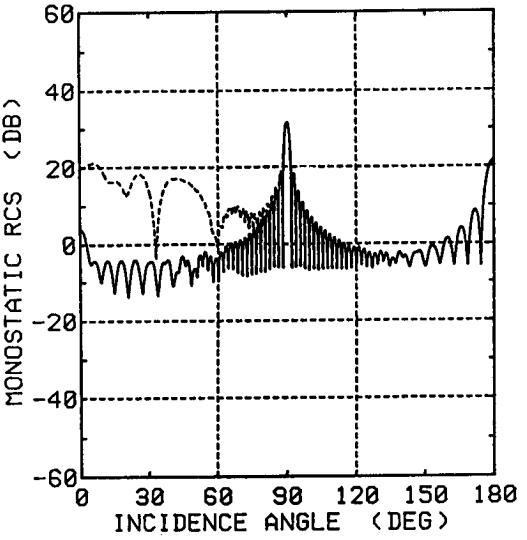

Figure 6b. Monostatic RCS σ/λ [dB] for $L/b = 3.0, 2b = 5\lambda$. Other particulars are the same as in Fig. 4a.

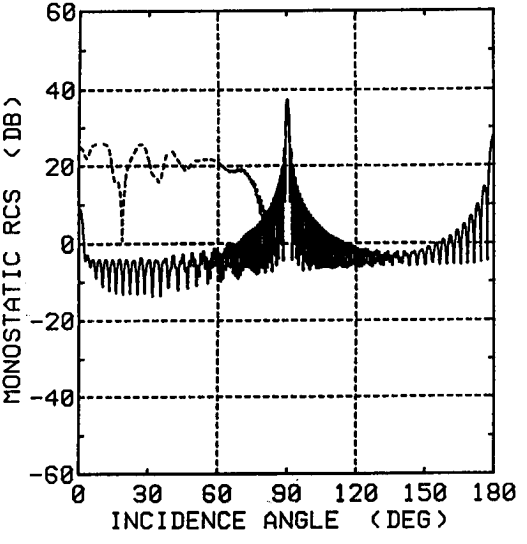

Figure 6c. Monostatic RCS σ/λ [dB] for $L/b = 3.0, 2b = 10\lambda$. Other particulars are the same as in Fig. 4a.

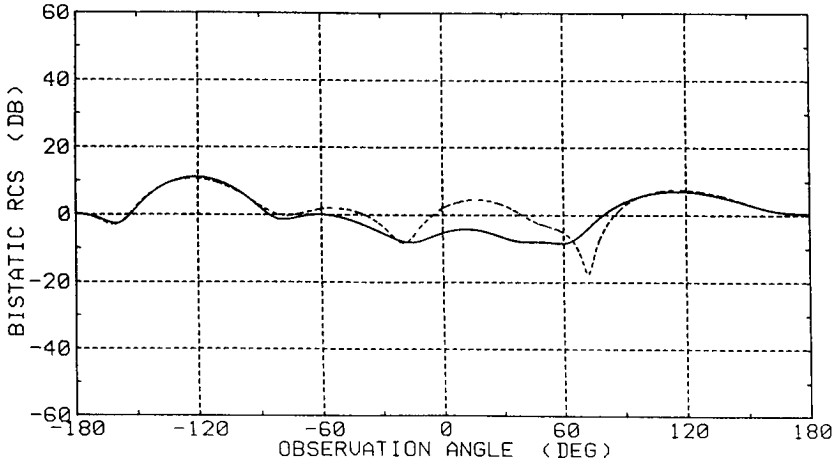

Figure 7a. Bistatic RCS σ/λ [dB] for $L/b = 1.0, 2b = \lambda, \theta_0 = 60°$. Solid lines and dashed lines denote the results for a material-loaded cavity with $\varepsilon_r = 2.5 + i1.25, \mu_r = 1.6 + i0.8$ and an empty cavity, respectively.

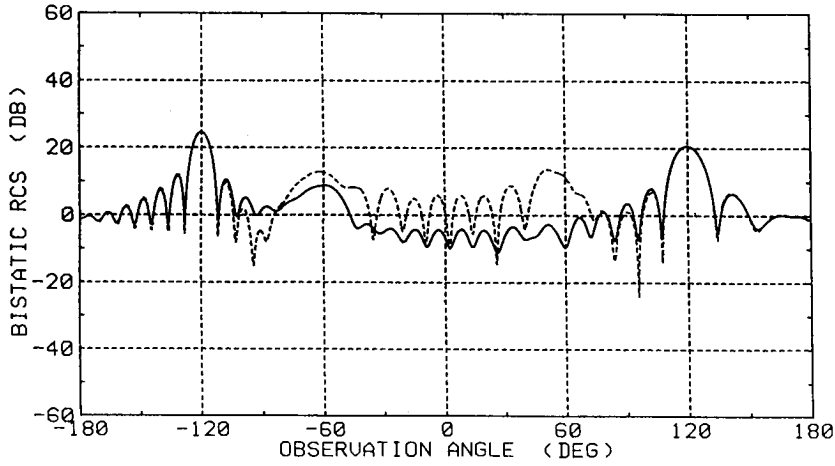

Figure 7b. Bistatic RCS σ/λ [dB] for $L/b = 1.0, 2b = 5\lambda, \theta_0 = 60°$. Other particulars are the same as in Fig. 7a.

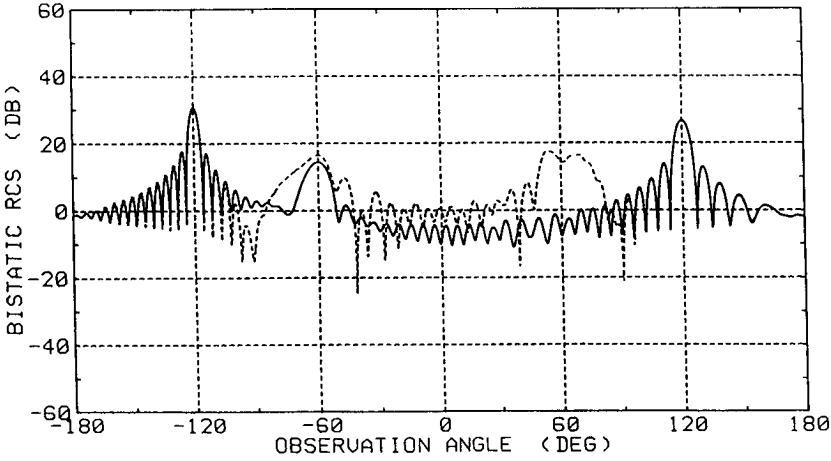

Figure 7c. Bistatic RCS σ/λ [dB] for $L/b = 1.0, 2b = 10\lambda, \theta_0 = 60°$. Other particulars are the same as in Fig. 7a.

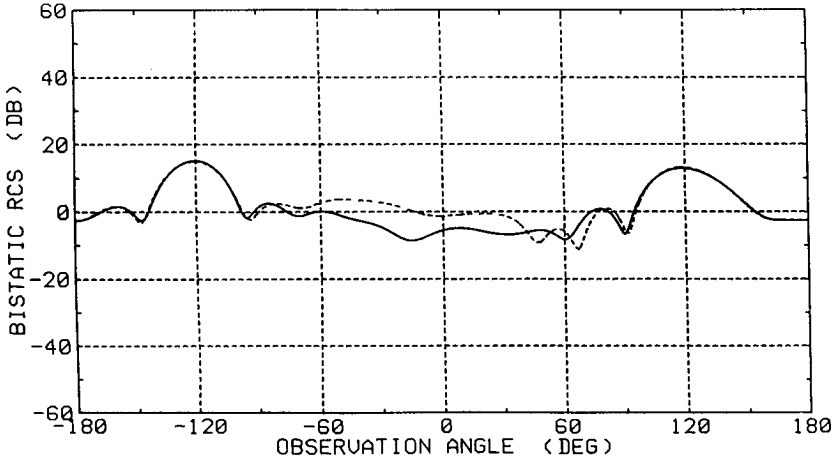

Figure 8a. Bistatic RCS σ/λ [dB] for $L/b = 2.0, 2b = \lambda, \theta_0 = 60°$. Other particulars are the same as in Fig. 7a.

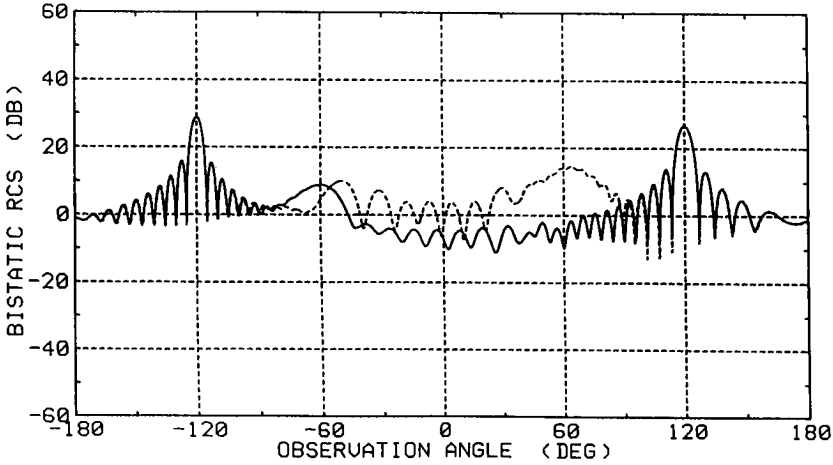

Figure 8b. Bistatic RCS σ/λ [dB] for $L/b = 2.0, 2b = 5\lambda, \theta_0 = 60°$. Other particulars are the same as in Fig. 7a.

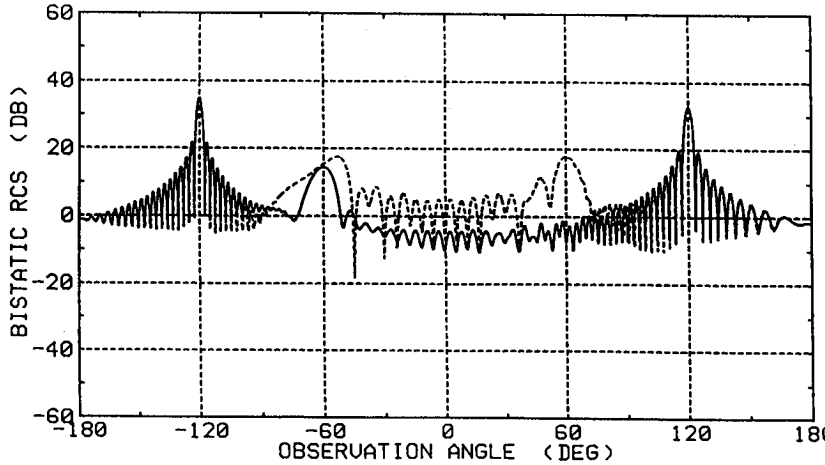

Figure 8c. Bistatic RCS σ/λ [dB] for $L/b = 2.0, 2b = 10\lambda, \theta_0 = 60°$. Other particulars are the same as in Fig. 7a.

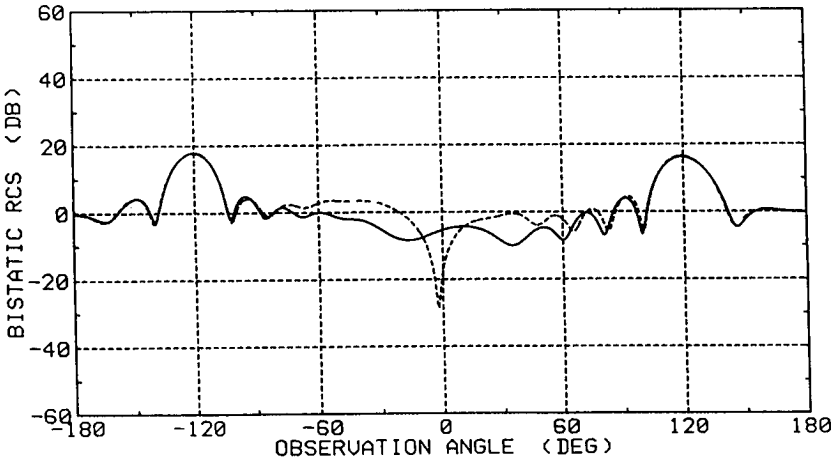

Figure 9a. Bistatic RCS σ/λ [dB] for $L/b = 3.0, 2b = \lambda, \theta_0 = 60°$. Other particulars are the same as in Fig. 7a.

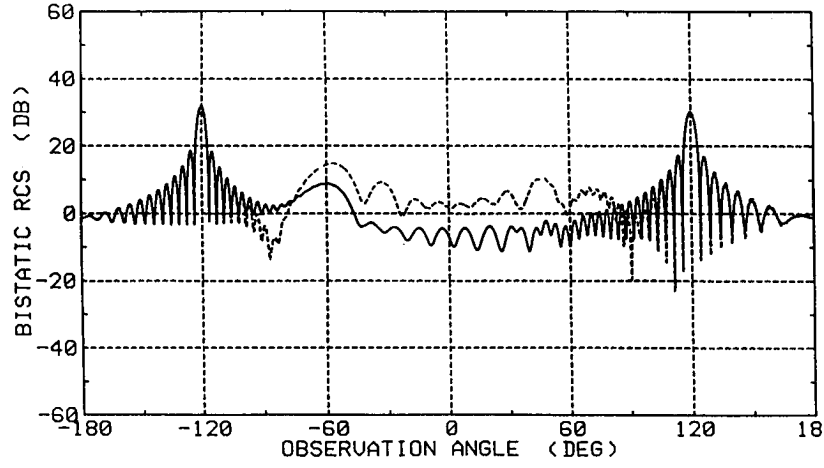

Figure 9b. Bistatic RCS σ/λ [dB] for $L/b = 3.0, 2b = 5\lambda, \theta_0 = 60°$. Other particulars are the same as in Fig. 7a.

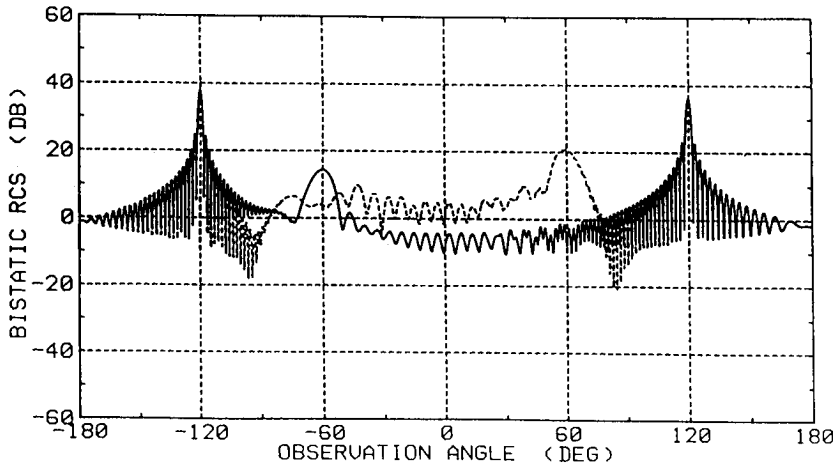

Figure 9c. Bistatic RCS σ/λ [dB] for $L/b = 3.0, 2b = 10\lambda, \theta_0 = 60°$. Other particulars are the same as in Fig. 7a.

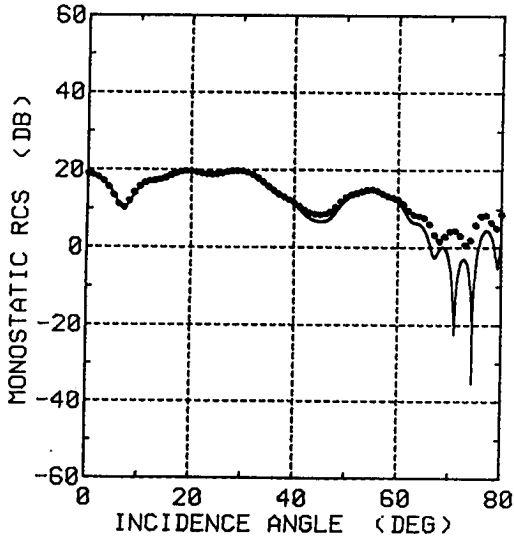

Figure 10a. Monostatic RCS σ/λ [dB] of an empty cavity with $L/b = 1.0$, $2b = 5\lambda$ and its comparison with Burkholder [29]. Solid lines and dots denote the results of this paper and Burkholder's results, respectively.

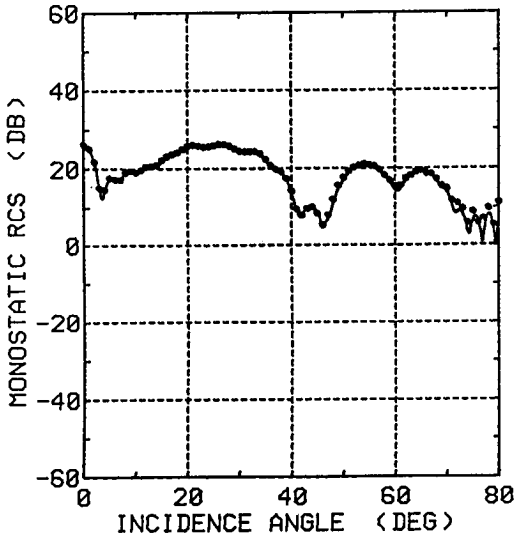

Figure 10b. Monostatic RCS σ/λ [dB] of an empty cavity with $L/b = 1.0$, $2b = 10\lambda$ and its comparison with Burkholder [29]. Other particulars are the same as in Fig. 10a.

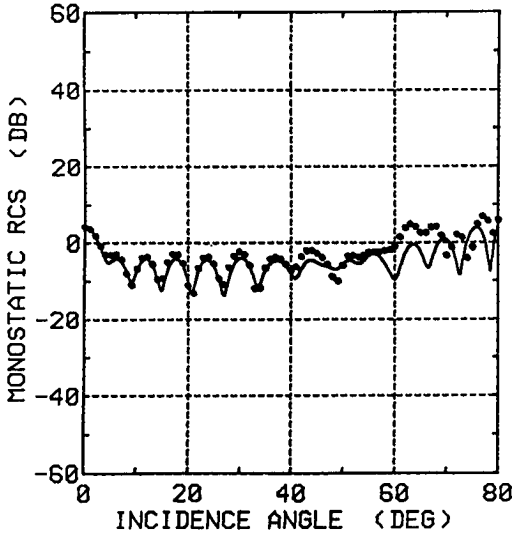

Figure 11a. Monostatic RCS σ/λ [dB] of a material-loaded cavity with $L/b = 1.0$, $2b = 5\lambda$, $\varepsilon_r = 2.5 + i1.25, \mu_r = 1.6 + i0.8$ and its comparison with Burkholder [29]. Other particulars are the same as in Fig. 10a.

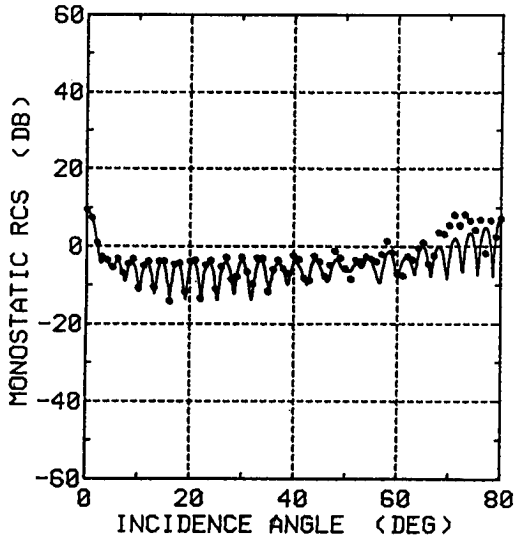

Figure 11b. Monostatic RCS σ/λ [dB] of a material-loaded cavity with $L/b = 1.0$, $2b = 10\lambda$, $\varepsilon_r = 2.5 + i1.25, \mu_r = 1.6 + i0.8$ and its comparison with Burkholder [29]. Other particulars are the same as in Fig. 10a.

We shall now make some comparisons with the other existing method. Recently Burkholder [29] obtained the monostatic RCS results for the same geometry using the hybrid asymptotic-modal approach [12, 15] together with the geometrical theory of diffraction (GTD). Shown in Figs. 10 and 11 are comparisons with the numerical data generated by Burkholder, where the results for both empty and loaded cavities are presented. In the figures, solid lines and dots denote the Wiener-Hopf results and Burkholder's results, respectively. Burkholder uses the hybrid asymptotic-modal approach for the scattering from the interior of the cavity, and the first order GTD for the external scattering from the leading edges at $z = L$ and the right-angled back corners at $z = -L$. In addition, for loaded cavities, his results are based on the use of the half-plane diffraction coefficient as an approximation, since the diffraction coefficients for an edge adjacent to a material region are not available. From Fig. 10 for empty cavities, we see that Burkholder's results with $2b = 5\lambda$ and 10λ agree very well with our Wiener-Hopf solution up to $\theta_0 = 60°$ and $70°$, respectively. The discrepancies near $\theta_0 = 80°$ are perhaps due to the fact that the effect of higher order diffraction by outer edges is not incorporated into his analysis. It is also interesting to note from Fig. 11 that, although the

half-plane diffraction coefficient is used in [29] as an approximation for loaded cavities, the agreement between the two methods is reasonably good.

11. Conclusions

As a generalization to the geometry treated in the previous papers, we have considered a parallel-plate waveguide cavity with dielectric/ferrite loading, and analyzed the E-polarized plane wave diffraction using the Wiener-Hopf technique. There are a number of analysis methods for treating cavity diffraction problems, but most of them do not rigorously take into account the scattering effect due to the exterior features of the cavity. Furthermore, the solutions deduced via these methods become less accurate when the size of the cavity tends to the low-frequency or the high-frequency limit. On the contrary, the Wiener-Hopf technique takes into account the edge condition rigorously and incorporates all the possible effects of the scattering from the interior and the exterior of the cavity. Hence, our final approximate solution presented in this paper is uniformly valid in incidence and observation angles as well as in cavity dimensions unless the cavity depth is too small compared with the wavelength. We have presented numerical examples of the monostatic RCS and the bistatic RCS for various physical parameters to discuss the scattering characteristics of the cavity in detail. As a result, it has been clarified that, for larger cavities, significant RCS reduction can be achieved by lossy material loading inside the cavity. Some comparisons with a high-frequency technique have also been given and the validity of that approach has been discussed briefly. A similar analysis for the case of H polarization is carried out in the companion paper [30].

Appendix

This appendix is concerned with asymptotic expansions of certain branch-cut integrals arising in the formal solutions of the Wiener-Hopf equations. The results presented here are due to Kobayashi [23, 26]. Let $f(\beta)$ be a function of a complex variable β satisfying the following conditions:

(i) *$f(\beta)$ is an analytic function of β, regular in $|\beta - k| < \varepsilon|k|$, where $k = k_1 + ik_2$ with $k_1 > 0$, $k_2 \geq 0$, and $\varepsilon \not\approx 0$.*

(ii) $f(\beta)$ *is* $O[(\beta-k)^{\delta}]$ *for any* β *such that* $|\beta-k| \geq R$ *with* $\varepsilon|k| < R < \infty$, *where* δ *is some real constant.*
(iii) $f(\beta)$ *is a continuous function of* β *on any bounded part of the semi-infinite straight path from* k *to* $k+i\infty$ *in the* β*-plane.*

Let α be a complex variable such that $|\alpha+k|>0$ and $-\pi/2 < \arg(\alpha+k) < 3\pi/2$, and introduce the function $F_{m\nu}(l,\alpha)$ as

$$F_{m\nu}(l,\alpha) = \frac{1}{\pi i}\int_{k}^{k+i\infty} e^{i\beta l}\frac{(\beta-k)^{\nu}f(\beta)}{(\beta+\alpha)^{m}}\,d\beta \qquad (A.1)$$

for $l>0$, $\operatorname{Re}\nu > -1$, and positive integer m, where $\arg(\beta-k)=\pi/2$. The conditions $l>0$ and $\operatorname{Re}\nu > -1$ ensure absolute convergence of the infinite integral in (A.1), whereas the conditions $|\alpha+k|>0$ and $-\pi/2 < \arg(\alpha+k) < 3\pi/2$ are required for avoiding the case where a pole of order m of the integrand at $\beta=-\alpha$ lies on the contour. The condition $\arg(\beta-k)=\pi/2$ has also appeared in the definition of $F_{m\nu}(l,\alpha)$, which has been introduced in order that $(\beta-k)^{\nu}$ be a single-valued function for non-integer ν.

Let us define the region D in the α-plane as follows:

$$D = \{\alpha\colon\ |\alpha+k|>0,\ -\pi/2 < \arg(\alpha+k) < 3\pi/2\}. \qquad (A.2)$$

Then it can be verified that $F_{m\nu}(l,\alpha)$ is uniformly convergent in α over any bounded closed region contained in D and hence, we find that $F_{m\nu}(l,\alpha)$ is an analytic function of α, regular in D. The following theorem now holds for the asymptotic expansion of $F_{m\nu}(l,\alpha)$ for large $|k|l$:

Theorem. *Under the conditions* (i)–(iii) *stated above,* $F_{m\nu}(l,\alpha)$ *can be expanded asymptotically as*

$$F_{m\nu}(l,\alpha) \sim \frac{e^{ikl}}{\pi}\sum_{n=0}^{\infty} f_n \frac{i^{\nu-m+n}}{l^{\nu-m+n+1}}\Gamma_m[\nu+n+1,-i(\alpha+k)l] \qquad (A.3)$$

for any $\alpha\in D$ *when* $kl\to\infty$, *where*

$$f_n = \frac{1}{n!}\frac{d^n f(\beta)}{d\beta^n}\bigg|_{\beta=k}, \qquad (A.4)$$

and $\Gamma_m(\cdot,\cdot)$ *is the generalized gamma function defined by* (98).

The above theorem is useful in accounting for the multiple edge diffraction explicitly in high-frequency range. Asymptotic expansions

of similar integrals have also been considered by Jones [31] and Williams [32], but their results are restricted to the special case where $\nu = \pm 1/2$ and $m = 1$ in $(A.1)$.

Acknowledgments

The authors would like to thank Professor Kazuo Horiuchi of Waseda University for many helpful discussions. They are also indebted to Dr. Robert J. Burkholder of The Ohio State University for providing the RCS data in Figs. 10 and 11. This work was supported in part by the 1992 Chuo University Special Research Grant.

References

[1] Knott, E. F., "A progression of high-frequency RCS prediction techniques," *Proc. IEEE,* Vol. 73, No. 2, 252–264, Feb. 1985.

[2] Knott, E. F., J. F. Shaeffer, and M. T. Tuley, *Radar Cross Section: Its Prediction, Measurement and Reduction,* Artech House, Boston, 1985.

[3] Knott, E. F., "Radar cross section," in *Aspects of Modern Radar,* Chap. 8, E. Brookner, Ed., Artech House, Boston, 1988.

[4] Lee, S.-W., and H. Ling, "Data book for cavity RCS: Version 1," *Tech. Rep.,* No. SWL89–1, Univ. Illinois, Urbana, Jan. 1989.

[5] Lee, S.-W., and R. J. Marhefka, "Data book of high-frequency RCS: Version 2," *Tech. Rep.,* Univ. Illinois, Urbana, Aug. 1989.

[6] Stone, W. R., Ed., *Radar Cross Sections of Complex Objects,* IEEE Press, New York, 1990.

[7] Bhattacharyya, A. K., and D. L. Sengupta, *Radar Cross Section Analysis and Control,* Artech House, Boston, 1991.

[8] Lee, C. S., and S.-W. Lee, "RCS of a coated circular waveguide terminated by a perfect conductor," *IEEE Trans. Antennas Propagat.,* Vol. AP–35, No. 4, 391–398, Apr. 1987.

[9] Altintas, A., P. H. Pathak, and M. C. Liang, "A selective modal scheme for the analysis of EM coupling into or radiation from large open-ended waveguides," *IEEE Trans. Antennas Propagat.,* Vol. AP–36, No. 1, 84–96, Jan. 1988.

[10] Ling, H., R.-C. Chou, and S.-W. Lee, "Shooting and bouncing rays: calculating the RCS of an arbitrary shaped cavity," *IEEE Trans. Antennas Propagat.*, Vol. AP–37, No. 2, 194–205, Feb. 1989.

[11] Ling, H., S.-W. Lee, and R.-C. Chou, "High-frequency RCS of open cavities with rectangular and circular cross sections," *IEEE Trans. Antennas Propagat.*, Vol. AP–37, No. 5, 648–654, May 1989.

[12] Pathak, P. H., and R. J. Burkholder, "Modal, ray, and beam techniques for analyzing the EM scattering by open-ended waveguide cavities," *IEEE Trans. Antennas Propagat.*, Vol. AP–37, No. 5, 635–647, May 1989.

[13] Ling, H., "RCS of waveguide cavities: a hybrid boundary-integral /modal approach," *IEEE Trans. Antennas Propagat.*, Vol. AP–38, No. 9, 1413–1420, Sept. 1990.

[14] Jeng, S.-K., "Scattering from a cavity-backed slit in a ground plane – TE case," *IEEE Trans. Antennas Propagat.*, Vol. AP–38, No. 10, 1523–1529, Oct. 1990.

[15] Pathak, P. H., and R. J. Burkholder, "High-frequency electromagnetic scattering by open-ended waveguide cavities", *Radio Sci,* Vol. 26, No. 1, 211–218, Jan.–Feb. 1991.

[16] Burkholder, R. J., R.-C. Chou, and P. H. Pathak, "Two ray shooting methods for computing the EM scattering by large open-ended cavities," *Computer Phys. Comm.*, Vol. 68, 353–365, 1991.

[17] Wang, T.-M., and H. Ling, "A connection algorithm on the problem of EM scattering from arbitrary cavities," *J. Electromagn. Waves Appl.*, Vol. 5, No. 3, 301–314, 1991.

[18] Noble, B., *Methods Based on the Wiener-Hopf Technique for the Solution of Partial Differential Equations,* Pergamon Press, London, 1958. See also, second edition, Chelsea Publishing, New York, 1988.

[19] Mittra, R., and S.-W. Lee, *Analytical Techniques in the Theory of Guided Waves,* Macmillan, New York, 1971.

[20] Kobayashi, K., "The Wiener-Hopf technique with applications to scattering and diffraction problems," in *A Course of Applied Mathematics,* Chap. 9 (in Japanese), K. Horiuchi, Ed., Corona Publishing, Tokyo, 1989.

[21] Kobayashi, K., "Wiener-Hopf and modified residue calculus techniques," in *Analysis Methods for Electromagnetic Wave Problems,* Chap. 8, E. Yamashita, Ed., Artech House, Boston, 1990.

[22] Kobayashi, K., and A. Sawai, "Plane wave diffraction by an open-ended parallel plate waveguide cavity," *J. Electromagn. Waves Appl.,* Vol. 6, No. 4, 475–512, 1992.

[23] Kobayashi, K., "Some diffraction problems involving modified Wiener-Hopf geometries," in *Analytical and Numerical Methods in Electromagnetic Wave Theory,* Chap. 4, M. Hashimoto, M., Idemen, and O. A. Tretyakov, Eds., Science House, Tokyo, 1993.

[24] Koshikawa, S., and K. Kobayashi, "Diffraction by a parallel-plate waveguide cavity with a thick planar termination," *IEICE Trans. Electron.,* Vol. E76–C, No. 1, 142–158, Jan. 1993.

[25] Meixner, J., "The behavior of electromagnetic fields at edges," *Res. Rep., Div. Electromagnetic Res., Inst. Math. Sci., New York Univ.,* No. EM–72, 1954. See also, J. Meixner, *IEEE Trans. Antennas Propagat.,* Vol. AP–20, No. 4, 442–446, July 1972.

[26] Kobayashi, K., "Plane wave diffraction by a strip: exact and asymptotic solutions," *J. Phys. Soc. Japan,* Vol. 60, No. 6, 1891–1905, June 1991.

[27] Kobayashi, K., "On generalized Gamma functions occurring in diffraction theory," *J. Phys. Soc. Japan,* Vol. 60, No. 5, 1501–1512, May 1991.

[28] Koshikawa, S., K. Kobayashi, and T. Eizawa, "Wiener-Hopf analysis of the high-frequency diffraction by a strip: higher order asymptotics," *Trans. IEE Japan,* Vol. 113–A, No. 3, 157–166, Mar. 1993 (in Japanese). See also, K. Kobayashi and S. Koshikawa, Symposium Record No. 5–26–6, Paper presented at *Symposium on Hyperbolic Partial Differential Equations and Its Applications to Mathematical Physics,* May 24–27, 1993, Osaka, Japan.

[29] Burkholder, R. J., private communication, Nov. 1992.

[30] Koshikawa, S., and K. Kobayashi, "Diffraction by a parallel-plate waveguide cavity with dielectric/ferrite loading: Part II – The case of H polarization," J. A. Kong, Ed., *Progress in Electromagnetics Research,* PIER 8, 427–458, 1994.

[31] Jones, D. S., "Diffraction by a wave-guide of finite length," *Proc. Camb. Phil. Soc.,* Vol. 48, 118–134, Jan. 1952.

[32] Williams, W. E., "Diffraction by two parallel planes of finite length," *Proc. Camb. Phil. Soc.*, Vol. 50, 309–318, Apr. 1954.